Geologic CO_2 storage in arkosic sandstones with $CaCl_2$-rich formation water

Wang Yanzhong[1*], Zan Nianmin[1], Cao Xu[2], Cao Yingchang[1], Yuan Guanghui[1], Jonathan Gordon Gluyas[2], Lin Miruo[1]

1. School of Geosciences, China University of Petroleum, Qingdao Shandong, 266580, China

2. Department of Earth Sciences, Durham University, Durham DH1 3LE, UK

* Corresponding author: Wang Yanzhong; E-mail address: wyzh@upc.edu.cn

Abstract: The feasibility of geologic CO_2 storage in deeply buried arkosic sandstones has been tested using high-temperature, high-pressure short-term laboratory experiments and long-term numerical simulations with CO_2-saturated solution rich in $CaCl_2$. These conditions mimic the conditions found today in the Eocene reservoir sandstones of depleted oilfields in the Dongying Sag, Bohai Bay Basin, China. Experiments at 100°C and 150°C and P_{CO2} of 4MPa were conducted on sandstones rich in K-feldspar and albite without anorthite. During the experiments, calcite and kaolinite precipitated whilst albite and K-feldspar partly dissolved. Ca^{2+} in formation water is shown to be critical for mineral trapping of CO_2. The continuous dissolution of K-feldspar and albite at a slow rate for a long time period can prolong duration time of calcite precipitation and increase geologic CO_2 storage capability by mineral trapping. Addition of NaCl, KCl and $MgCl_2$ can prolong the dissolution time of K-feldspar and albite and precipitation duration of calcite. It also increased the mass of sequestered CO_2 by mineral trapping. The process of geologic CO_2 storage can be divided into 3 stages. In stage I, calcite precipitates rapidly, and geologic CO_2 storage is dominated by solubility trapping within 100 years. Stage II lasts up to 300 years in the solution without NaCl, KCl and $MgCl_2$ and 900 years with addition of NaCl, KCl and $MgCl_2$ into the solution. The precipitation rate of calcite decreases abruptly and the mass of mineral trapping of CO_2 increases with increasing time, because dissolution of K-feldspar and albite causes decrease of Ca activity and prolongs calcite precipitation time. The geologic CO_2 storage is dominated by mineral trapping. In stage III, reactions reach equilibrium and the mass of geologic CO_2 storage reaches the maximum. The calculated mass of CO_2 by mineral trapping in sandstones of the Es4x to Es3z in the Dongying Sag is about 3.61GT.

Keywords: geologic CO_2 storage; mineral trapping; K-feldspar- and albite-rich sandstones; $CaCl_2$-rich formation water; laboratory experiment; numerical simulation.

Introduction

Carbon Capture and Storage (CCS) is a practical technology to create new and sustainable CO_2 sinks (Gluyas and Mathias, 2013; Leung et al., 2014; Elmabrouk et al., 2017). Geologic CO_2 storage is currently considered to be the most viable for the permanent storage of the large quantities of CO_2 (Celia and Nordbotten, 2009; Zwaan and Semkens, 2009; Yang et al., 2010; Myer, 2011). The geologic CO_2 storage mainly involves injection of CO_2 into depleted oil and gas reservoirs, deep saline aquifers, and possibly mined and unmined coal seams (Wigand et al., 2008; Yu et al., 2015,

2017). The geologic CO_2 storage potential in depleted oil and gas reservoirs can reach 920 GT in the largest 155 petroleum provinces that encompass 32,000 known oil and gas fields (Klett et al., 1997; Masters et al., 1998; Stevens et al., 2001; *International Energy Agency Report, 2004*). Therefore, injection of CO_2 into depleted oil and gas fields with good sealing conditions, high porosity and permeability has become a major research theme for geologic CO_2 storage, although at present only about 5 million tons of CO_2 is stored each year using this technology (Jenkins et al., 2012; De Coninck and Benson, 2014).

The geologic CO_2 storage mechanisms include physical trapping, residual saturation trapping, solubility trapping and mineral trapping (Bachu et al., 2007; Matter and Kelemen, 2009; Shukla et al. 2010; Li et al., 2016; Li et al., 2018). The mineral trapping is the safest and most stable geologic CO_2 storage mechanism in the long term (He et al., 2015; Munz et al., 2012; Alia et al., 2015; Yang et al., 2017). However, most research on geologic CO_2 storage mechanisms in depleted oil and gas fields are currently focused mainly on physical trapping and solubility trapping (Gilfillan et al., 2009). Mineral trapping of CO_2 in depleted oil and gas fields is important for permanent storage (Gunter et al., 2000; Raistrick et al., 2009; Matter and Kelemen, 2009; Scislewski and Zuddas, 2010; Lu et al., 2010, 2014; Luquot et al., 2012; Carroll et al., 2013b; Luhmann et al., 2012; Kirsch et al., 2014).

Mineral trapping of CO_2 primarily refers to carbonation of CO_2 to form calcite, dolomite (Li et al., 2009; Hangx and Spiers, 2009; Li and Pang et al., 2017). The sources of Ca^{2+} and Mg^{2+} is a key factor for carbonation of CO_2 (Gilfillan et al., 2009; Matter and Kelemen, 2009). At present there are trials in which CO_2 is injected into igneous rocks and anorthite-rich clastic rocks. The injected CO_2 reacts with divalent cations of Ca^{2+}, Mg^{2+} from dissolution of olivine, pyroxene, and anorthite in igneous rocks to form magnesium/calcium carbonates (Mcgrail et al., 2006; Aradóttir et al., 2011; Kumar et al., 2017; Li and Li et al., 2017; Wolff-Boenisch and Galeczka, 2018). However, the mass of mineral trapping of CO_2 in igneous rocks is only ever likely to be very small due to small volumes of fractures in such rocks and upon which permeability depends (Van Pham et al., 2012). After injection of CO_2 into anorthite-rich clastic rocks, the injected CO_2 reacts with the calcium from anorthite dissolution at low pH to form calcite (Hitchon et al., 1999; Xu et al., 2004; Gilfillan et al., 2009; Matter and Kelemen, 2009; Gaus, 2010; Liu et al., 2011; Munz et al., 2012). However, most clastic rocks in depleted oil and gas fields lack calcium-containing minerals.

Previous studies suggested that solubility trapping is the major mechanism of geologic CO_2 storage in clastic rocks lacking calcium-containing minerals (Gilfillan et al., 2009; Matter et al., 2016; Hellevang et al. 2014). Therefore, geologic CO_2 storage by mineral trapping in clastic rocks lacking calcium-containing minerals needs to be further investigated because of the vast pore volume available for storage. Whilst calcium-bearing silicate minerals are relatively rare in sandstones, calcium-rich connate brines (pore water) is relatively common and as such we have investigated the

role that it may place in sequestration of CO_2 through mineralization. In the oilfields in eastern China, the sandstones are dominantly rich in K-feldspar and albite without anorthite (Li et al., 2009; Yuan et al., 2015a), but the formation water is mainly rich in $CaCl_2$ (Yuan et al., 2015a, 2015c; Li and Pang et al., 2017). Thus, the oilfields of eastern China are a good location for study of geologic CO_2 storage (Li et al., 2016; Yuan et al., 2017a).

We combined laboratory experiments and numerical simulations, constrained by the conditions within the Eocene sandstones of the Shengtuo area, Dongying Sag, Bohai Bay Basin, China, in a single study to (1) discuss mineral trapping of CO2 with CaCl2 in formation water as the calcium source, (2) analyze of the influence of K-feldspar and albite dissolution on mineral trapping of CO2, (3) improve the understanding of geologic CO2 storage processes, and (4) estimate capability of geologic CO2 storage in the sandstones rich in K-feldspar and albite with formation water rich in CaCl2.

1. Geological setting

The lower part of the fourth Member of the Paleogene Shahejie Formation (Es4x) to the middle part of the third Member of the Paleogene Shahejie Formation (Es3z) in the Shengtuo area are the target of this study. The regional tectonic background and stratigraphic development of the Dongying Sag were referred to Yuan & Wang (2001) and Cao et al (2018). The rocks are dominated by conglomerates and sandstones. The sandstones are dominated by lithic feldsarenite and feldspathic litharenite. The feldspars are mainly K-feldspar and albite without anorthite. Carbonate cements, quartz overgrowth, kaolinite and illite are the main authigenic minerals in the sandstones. The present-day formation temperature is approximately 150°C at 4000 m and approximately 82°C at 2000 m (Wang, 2010; Guo et al., 2012). The P_{CO2} in hydrocarbon reservoirs ranges from 0.25 MPa at 2000m to 4.05 MPa at 4000m (Yuan et al., 2015a). The formation water is highly saline, and the concentrations of Ca^{2+}, Mg^{2+}, K^{+}, Na^{+} are 13.85~26.26 g/L, 0.71~1.91 g/L, 0.52~0.71 g/L, 56.65~100.43 g/L, respectively (Yuan et al., 2015a and 2015b). The average concentration of $CaCl_2$ in the formation water in the fourth Member of the Paleogene Shahejie Formation (Es4) is 0.38 mol/L. Core-analysis porosities of sandstones range from 2.4% to 35% with an average of 12.76%. Porosities of oil layers mostly fall between 11% and 35% with an average of 25.55%.

2. Methodology

2.1 Laboratory experiments

Six laboratory experiments (LES) on the reaction of CO_2-saturated solution and sandstones rich in K-feldspar and albite were conducted at China University of Petroleum (UPC). The experimental apparatus is composed of a high-pressure and high-temperature resistant stainless-steel alloy reactor, carbon dioxide cylinder, heating cover, temperature and pressure sensors and temperature-pressure control system (Fig. 1). The reactor with volume of 500ml is equipped with a Ti-Ni-Cr alloy wall and

a netted cradle. CO_2 with a purity of more than 99.995% was injected into the reactor by pumping to reach the designed P_{CO2} of 4.0 MPa. The real-time temperature and pressure were monitored by a sensor connected with a digital thermometer and a pressure meter. Temperature was adjusted by an automatic control instrument, with an error of ± 1°C.

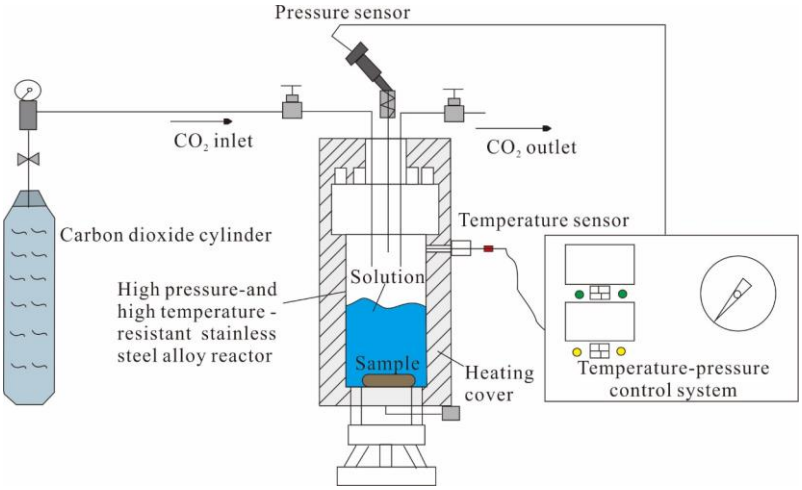

Fig. 1. Experimental apparatus used for the laboratory experiments

Two pieces of typically sandstones rich in K-feldspar and albite were taken from the Es3z at 2938.13m in well Tuo76 and from the Es4x at 3671.8m in Well Tuo720 in the Shengtuo area, respectively. The Es4x sandstone sample was cut into six small pieces. Mineral composition of the six sandstone samples were determined by X-ray diffraction (XRD) in the College of Chemical Engineering, UPC. The six pieces of sandstone samples were cut into small round slabs with a diameter of 25mm and a thickness of 3mm. The surfaces of the round slabs are uneven (Fig. 2a). One surface of each round slab was polished to be smooth and flat (Fig. 2b) and washed repeatedly in deionized water.

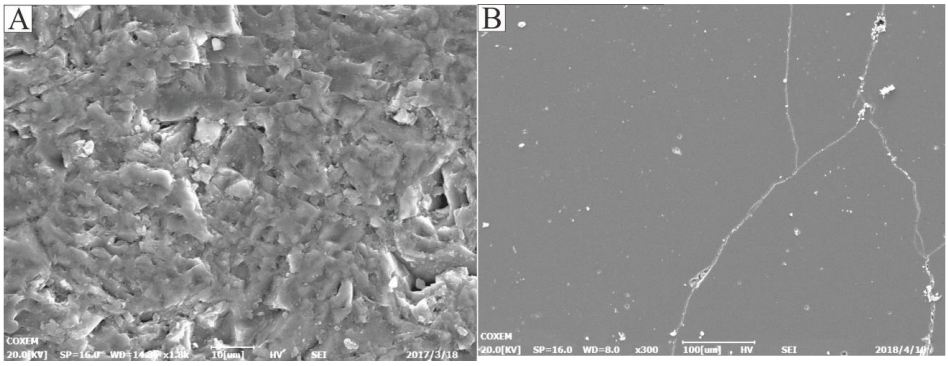

Fig. 2. SEM photomicrographs showing (A) the uneven surface of unpolished pre-experiment sample and (B) the smooth and flat surface of polished pre-experiment sample, 2938.13m, Well Tuo76.

The experimental process is as follow. (1) The prepared sandstone sample was placed at the bottom of the reactor, 200ml of solution was poured into the reactor, and then the reactor was sealed. (2) CO_2 was continuously injected into the reactor by pumping, to maintain P_{CO2} of 4.0±0.1 Mpa in reaction system and to ensure CO_2 saturation during the whole experiments. (3) The reactor was heated to 100°C and 150°C with a heating rate of 4°C/min, continuing 48h and 96h, respectively.

The experimental conditions and processes are shown in Table 1. The ion concentration in SHCa-LE and FW-LE was determined according to the average ion concentration in formation water in the Es4x to Es3z in the Shengtuo area (Table 2). The rock composition and mineral composition of DLF-LE and FL-LE will be introduced in the section of mineralogy.

After the laboratory experiments, the reactors were quenched to room temperature in cold water for 10 minutes. The reaction solution was extracted by a syringe and put into a sealed glass vial. The reaction solution was filtered before ion concentration can be tested. The concentrations of Al^{3+}, SiO_2(aq), K^+, Na^+, Ca^{2+} in the six post-experiment solution samples were tested using an ICP-MS (Thermo icapQ, USA) in the Analytical and Measurement Research Center, Qingdao Institute of Oceanology. The analysis error of cations was less than 0.001ppm. The pH of all the post-experiment solution samples was analyzed by pHS-3C of Rex (Shanghai) in the College of Chemical Engineering, UPC. The analysis error of multi-measurements for pH at 25°C was scaled between -1% and 1%. The concentrations of HCO_3^- and CO_3^{2-} were calculated by pH and dissociation constants of HCO_3^- and CO_3^{2-} referred to Li and Duan (2007). Saturation indices for different minerals were calculated according to the measured temperatures (T), pressures (P), and chemical composition of post-experiment solution. Saturation index is defined as lg (Q/K_{eq}), where Q denotes the activity quotient and K_{eq} denotes the equilibrium constant. Equilibrium constants (Keq) are different at different temperatures (Table 3).

The post-experiment samples were repeatedly cleaned in deionized water to remove experimental liquid and then were observed under a Coxem-30plus SEM to identify dissolution and precipitation of minerals. The chemical composition of minerals in the post-experiment samples was tested under a Bruker Energy Dispersive Spectrometer System (EDS) (X-Flasher Detector 430-M).

2.2 Numerical simulations

With the laboratory experimental results used as constraining conditions, five numerical simulations (NSS) on the long-term reaction of CO_2-saturated fluid and sandstones rich in K-feldspar and albite were conducted using the react module in the Geochemist's Workbench (GWB) 9.0.

The conditions of numerical simulations are listed in Table 4. The fluid chemistry and mineral composition data are listed in the Tables 5 and 6. The temperature and pressure conditions are the same as those in the laboratory experiments (Table 4). The volume fraction of DLF-NS and FL-NS were from the mineral composition of DLF-LE and FL-LE in the laboratory experiments (Table 5 and Table 8). The volume fraction of DLF-NS1 was determined by the average mineral composition of the sandstones in the Es4x to Es3z in the Shengtuo area (Table 5). The rock composition and mineral composition of DLF-NS1 will be introduced in the section of mineralogy(Table 5). The ion composition of SHCa-NS and FW-NS was from the ion concentration of SHCa-LE and FW-LE in laboratory experiments (Table 6). The water: rock ratio is discussed in Appendix 3 and Table 5. The

numerical simulations runs under the closed system. Any external water was not added in the numerical simulations.

Constraints such as K_{25}, E_a, A_m for K-feldspars, albite, dolomite, calcite, kaolinite and quartz are available in Table 7 and Table 17 in Appendix 3. The reaction rate of kinetically-controlled reaction of CO_2-saturated fluid and sandstones rich in K-feldspar and albite is referred to Lasaga, A. C.(1981), Aagaard, P. & Helgeson, H.C. (1982) and Xu et al (2005). The rate constant of aluminosilicate and carbonate minerals is a function of temperature (Perkins & Gunter, 1995; Gunter et al., 1997; Xu et al., 2005).

The reaction path determined by laboratory experiments was used as the constraint condition in numerical simulations. The reaction path will be discussed at the discussion section of this paper. The boundary conditions for numerical simulations are listed in Appendix 2. The model of the CO2 solubility and activity are introduced in Appendix 3.

3. Results

3.1 Mineralogy

XRD data of mineral composition show that the sandstones in the Es4x to Es3z are rich in K-feldspar and albite. K-feldspar content is 2-27% with an average of 11%. albite content is 2%-46% with an average of 24%. Quartz content is 3%-63% with an average of 39%. Kaolinite content is 0-9% with the average of 1.7%. Dolomite content is 0-45% with the average of 7%. XRD analysis of DLF-LE shows that the volume fraction of K-feldspar, albite, quartz, kaolinite, and dolomite is 8%, 18%, 40%, 0.99% and 33%, respectively (Table 8). XRD data of the FL-LE shows that the volume fraction of K-feldspar, albite, quartz, and kaolinite is 22%, 24%, 52% and 2%, respectively (Table 8).

The samples are Medium and coarse-grained sandstones. The grain sizes of sandstone samples are analyzed by SEM and thin sections (methodology referred to Sundal & Hellevang (2019)). The sand fraction is classified as quartz, K-feldspar, albite, and lithic fragments from fine to coarse. Albite is the most reactive phase in Medium and coarse-grained sand fractions. K-feldspar and quartz are finer in the fine and medium-grained sand fractions. The dolomite cements mainly appear as poikilotopic blocks and locally as pore-filling crystals. It does not block silicate mineral surfaces.

3.2 Laboratory experiments

3.2.1 Dissolution of detrital grains and dolomite cements

The degree of dissolution for different minerals on the surfaces of the post-experiment samples is significantly different. The dissolution of albites is stronger than that of K-feldspars, and the dissolution of quartz is weakest. A few etch pits (<2μm in diameter) on the surfaces of quartz grains were observed. (Fig. 3).

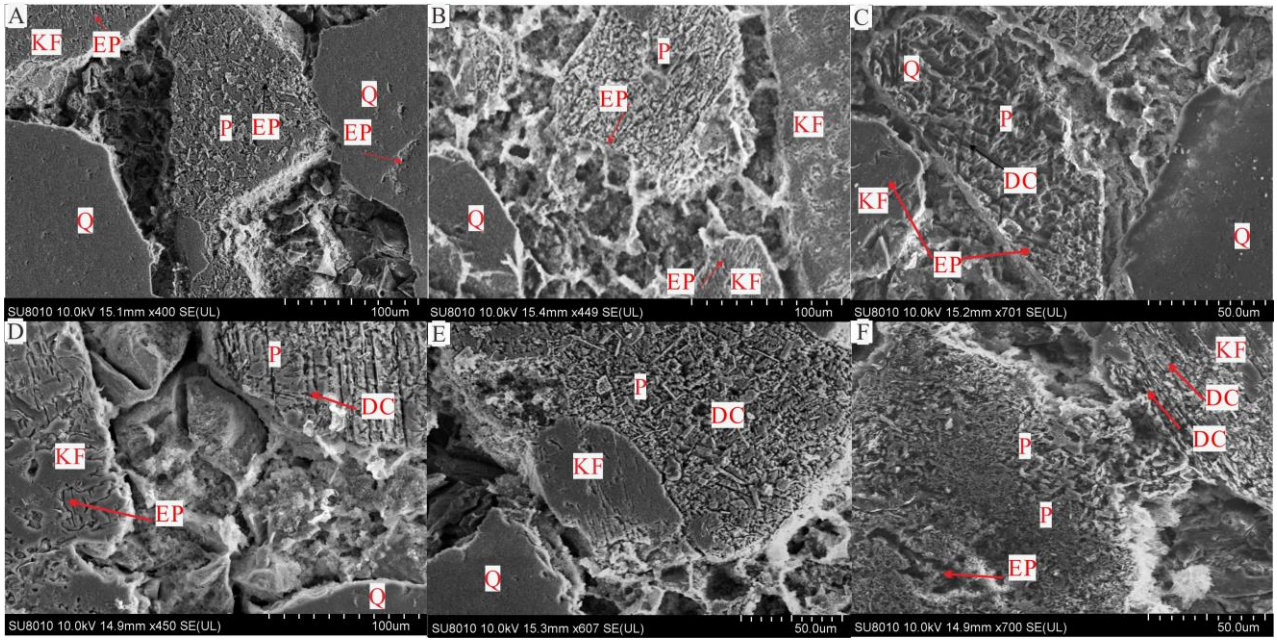

Fig. 3. SEM photomicrographs showing etch pits on the surfaces of albites, K-feldspars and quartzes. (A), (B), (C), (D), (E) and (F) are the post-experiment samples from laboratory experiments 1, 2, 3, 4, 5, and 6, respectively. Q, quartz; KF, K-feldspar; P, albite; EP, etch pits; DC, dissolution along cleavage.

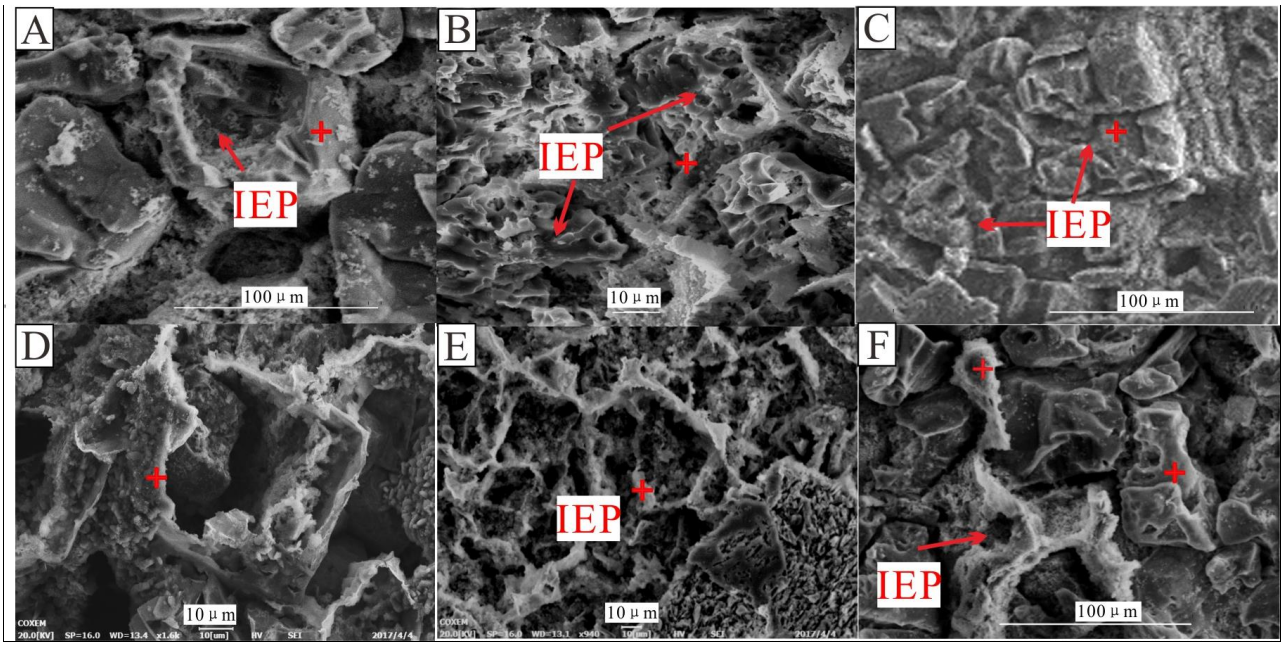

Fig. 4. SEM photomicrographs and EDS analyses showing irregular etch pits on the surfaces of the dolomite cements in the post-experiment samples from the (A) laboratory experiment 1, (B) laboratory experiment 2, (C) laboratory experiment 3, (D) laboratory experiment 4, (E) laboratory experiment 5, and (F) laboratory experiment 6. The red crosses represent the locations of EDS analysis. IEP, Irregular etch pits.

In laboratory experiment 1, many scattered etch pits (3~4μm in diameter) occured on the surfaces of the albite grains and weak corrosion on the edges of K-feldspars grains (Fig. 3A). In laboratory experiment 2, the irregular etch pits (6~7μm in diameter) developed extensively on the albite surfaces of the post-experiment sample (Fig. 3B). Compared with laboratory experiment 1, the dissolution degree of K-feldspar was significantly increased in laboratory experiment 2 (Fig. 3A, B). The larger corrosion pits (greater than 10μm in diameter) were observed on the surfaces of K-feldspar grains and albite grains in the post-experiment samples of the laboratory experiments 3, 4, 5, 6 at 150 °C for 4 days (Fig. 3C, D, E and F). The dissolution of albite grains at 150°C for 4 days in the

laboratory experiments 3, 4, 5, 6 strengthened dramatically and was stronger along cleavages (Fig. 3C, D, E and F). The dissolution of K-feldspar grains at 150°C for 4 days in the laboratory experiments 3, 4, 5, 6 was stronger than that of K-feldspar grains at 150°C for 2 days in the laboratory experiments 1, 2 (Fig. 3A, B).

A large number of irregular etch pits were developed on the surfaces of most dolomite cements in the post-experiment samples (Fig. 4 A and B; Table 9).

3.2.2 Precipitation of authigenic minerals

No authigenic minerals were found in the post-experiment sample from the laboratory experiment 1. Small hexagon-shaped authigenic minerals (Fig. 5 A-E), with cross sectional diameter (d) of less than 0.5μm and height (h) of about 0.1μm, covered approximately 5% of the feldspar surfaces in the post-experiment sample from the laboratory experiments 2 and about 10% of the feldspar surfaces in the post-experiment samples from the laboratory experiments 3, 4, 5, 6. In addition, a large amount of lath-shaped authigenic minerals (Fig. 5E and F) were precipitated on the surfaces of the albite grains in the post-experiment samples from the laboratory experiments 4 and 6. The hexagon-shaped authigenic minerals are mainly composed of O, Si and Al (Fig. 5A-E; Table 9), suggesting these minerals are probably kaolinite particles. The lath-shaped authigenic minerals are mainly composed of O and Al (Fig. 5C and F; Table 9), suggesting these minerals are probably gibbsite particles. The relative abundance of authigenic minerals on the feldspar surfaces from each laboratory experiment is consistent with observed distribution of mineral dissolution.

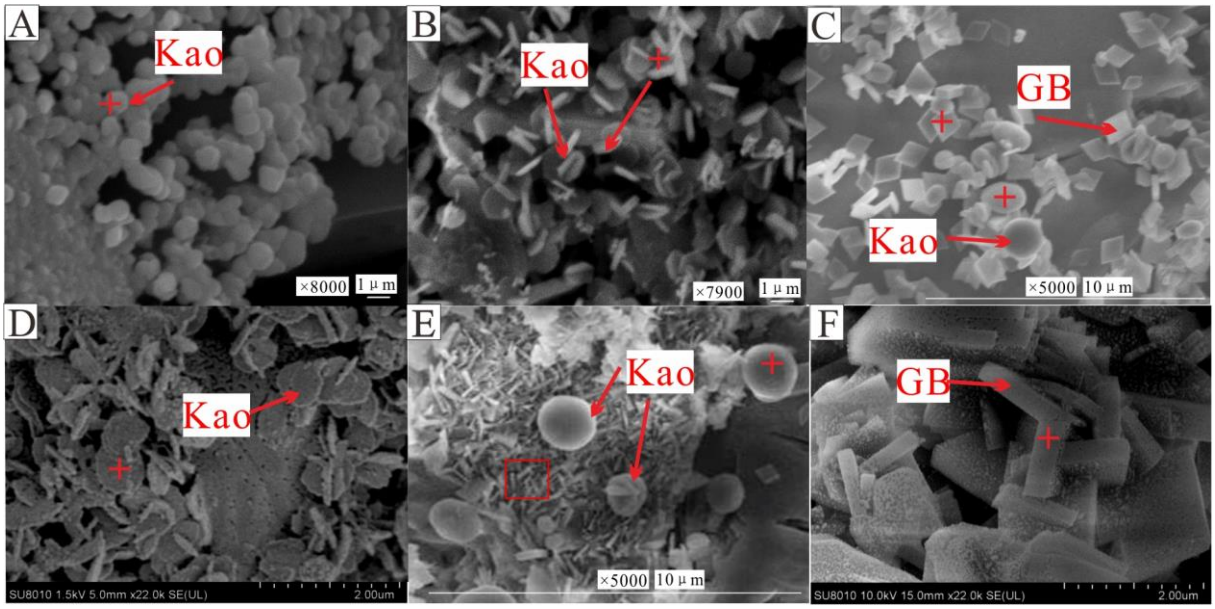

Fig. 5. SEM photomicrographs and EDS analysis of authigenic minerals in the post-experiment samples. (A) Hexagon-shaped authigenic minerals(with cross sectional diameter (d) of less than 0.5μm and height (h) of about 0.1μm) on the surface of feldspar in the post-experiment sample from the laboratory experiment 2; (B) Small hexagon-shaped authigenic minerals in the post-experiment sample from the laboratory experiment 3; (C) Hexagon-shaped and short lath-shaped authigenic minerals on the surface of feldspar in the post-experiment sample from the laboratory experiment 4; (D) Hexagon-shaped authigenic minerals in the post-experiment sample from the laboratory experiment 5; (E) Hexagon-shaped minerals on the surface of the albite grains in the post-experiment sample from the laboratory experiment 6; The red box is the location of photomicrograph F; (F) short lath-shaped minerals on the surface of the albite grains in the post-experiment sample from the laboratory experiment 6. The red crosses represent the locations of EDS analysis. Kao, Kaolinite. GB, Gibbsite.

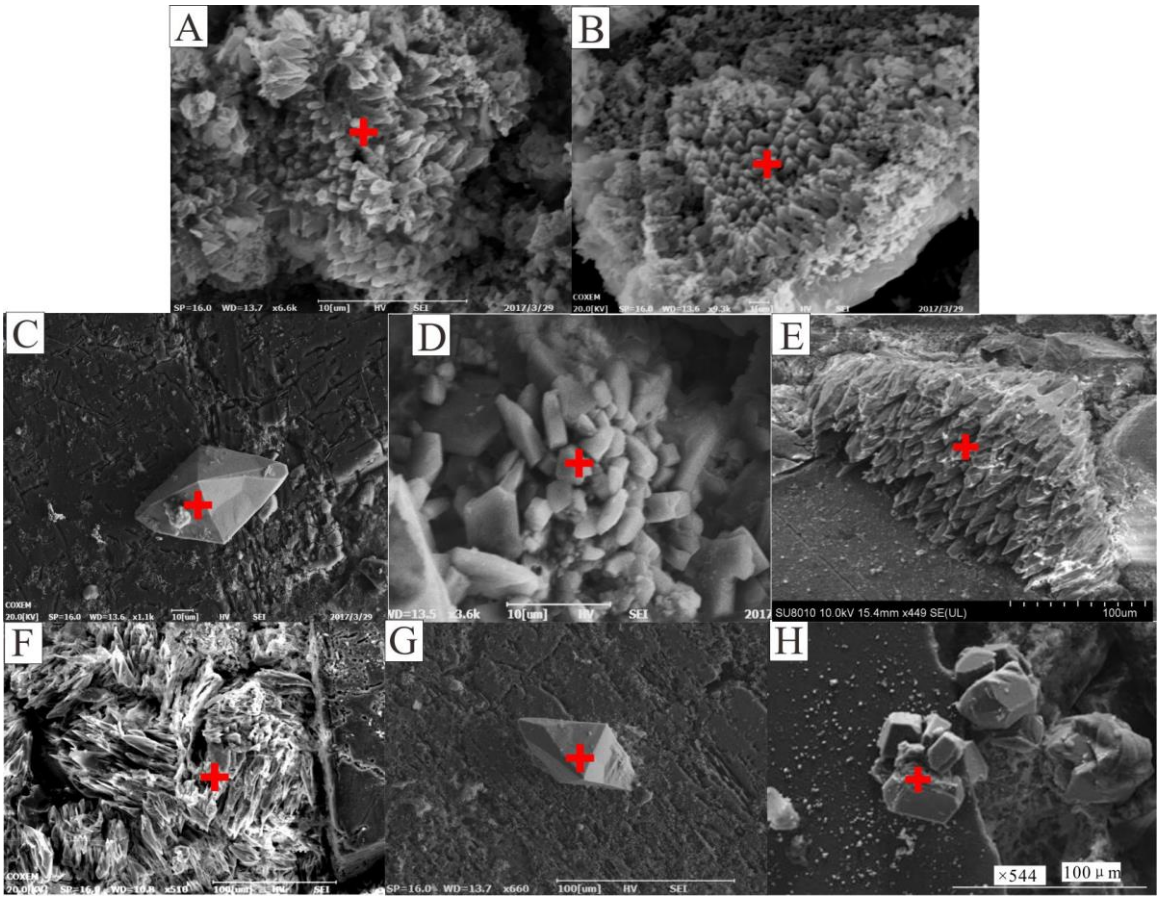

Fig. 6. SEM photomicrographs and EDS analysis of authigenic minerals in the post-experiment samples. (A) Crystalline cone of authigenic minerals precipitated in the laboratory experiment 2; (B) Crystalline cone of authigenic minerals precipitated in the laboratory experiment 3; (C) Rhombohedral authigenic minerals precipitated on the surfaces of K-feldspar in the laboratory experiment 3; (D) Short columnar authigenic minerals precipitated between detrital grains in the laboratory experiment 3; (E) Crystalline cone of authigenic minerals precipitated in the laboratory experiment 5; (F) Crystalline cone of authigenic minerals precipitated in the laboratory experiment 6; (G) Rhombohedral authigenic minerals precipitated on the surface of quartz in the laboratory experiment 5; (H) Blocky minerals precipitated on the surface of quartz in the laboratory experiment 6. The red crosses represent the locations of EDS analysis.

Crystalline cone of authigenic minerals, rhombohedral minerals and short columnar crystal minerals were precipitated on the surfaces of K-feldspar, albite and quartz in the laboratory experiments 2, 3, 5, 6 (Fig. 6). These newly precipitated minerals are mainly composed of O, C, Ca (Fig. 6B, C, E, G, H; Table 9), showing these minerals are probably calcite particles. The crystalline cone minerals and blocky minerals were also precipitated between detrital grains (Fig. 6A, D, F). The volume of the calcite precipitated in the laboratory experiments 5 and 6 is larger than laboratory experiment 3. These minerals between detrital grains are composed of O, C, Ca, reflecting that they are also likely to be calcites (Fig. 6A, B, E-H; Table 9).

3.2.3 Chemical composition of the post-experiment solution

In the three deionized water experiments 1, 2 and 3, pH and concentration of Al^{3+}, K^{+}, Na^{+} and SiO_2(aq) increased with the increase of reaction time and temperature (Table 10). Comparing laboratory experiment 1 with laboratory experiment 2, it was found that the concentration of Ca^{2+}, Fe^{2+}, Mg^{2+}, HCO_3^{-} and CO_3^{2-} decreased obviously with the increase of temperature from 100°C to 150°C (Table 10). Comparing laboratory experiment 2 and laboratory experiment 3, the concentration

of Ca^{2+}, Fe^{2+}, Mg^{2+}, HCO_3^- and CO_3^{2-} increased with the increase in reaction time from 2 days to 4 days (Table 10). Compared with laboratory experiments 1, 2 and 3, pH and concentration of Al^{3+}, $SiO_2(aq)$, HCO_3^- and CO_3^{2-} of the post-experiment solution in the laboratory experiments 4, 5 and 6 were lower, whereas the concentration of Ca^{2+}, Mg^{2+}, Fe^{2+}, K^+, and Na^+ was higher (Table 10).

The calculated saturation indices of all the post-experiment solutions in the laboratory experiments 1 and 2 indicate that the solutions were under-saturated with respect to K-feldspar, albite, quartz, dolomite (SI<0) and saturated with respect to kaolinite, gibbsite, calcite (SI>0) (Table 11). In the Laboratory experiments 3, 4, 5 and 6 at 150℃ for 4 days, the post-experiment solution was close to equilibrium with respect to quartz (−0.4<SI<−0.1), saturated with respect to calcite, kaolinite, gibbsite and under-saturated with respect to dolomite, K-feldspar and albite (Table 11).

3.4 Numerical simulations

3.4.1 Fluid chemistry

The species concentration of $CO_2(aq)$ was stable with the increase of numerical simulation time (Fig. 7 A, E) in all numerical simulations. The results of all the numerical simulations show that 1000 years after CO_2 injection at 150℃ and P_{CO2} of 4MPa, the total concentration of CO_2 dissolved into formation water in the form of $CO_2(aq)$, CO_3^{2-} and HCO_3^- was 0.449 mol/L in numerical simulations 1, 0.456 mol/L in numerical simulations 2, 0.72mol/L in numerical simulations 3, 0.472mol/L in NS 4, 0.473mol/L in numerical simulations 5, respectively (Table 12). The concentration of $CO_2(aq)$, CO_3^{2-} and HCO_3^-in the formation water in all the numerical simulations was shown in Table 12.

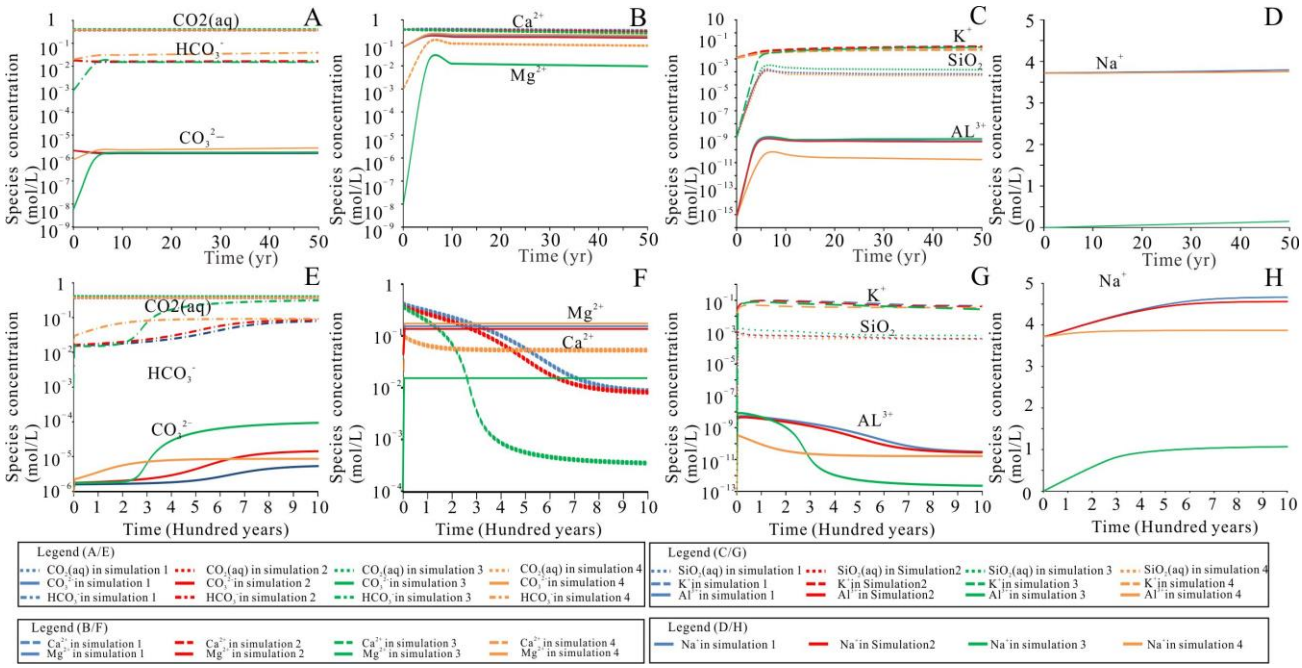

Fig. 7. Changes in species concentration with simulation time in all numerical simulations from 0 to 50 years. (A) changes in species concentration of $CO_2(aq)$, CO_3^{2-}, HCO_3^- from 0 to 50 years; (B) changes in species concentration of Ca^{2+}, Mg^{2+} from 0 to 50 years; (C) changes in species concentration of $SiO_2(aq)$, K^+, Al^{3+} from 0 to 50 years. (D) changes in species concentration of Na^+ from 0 to 50 years. (E) changes in species concentration of $CO_2(aq)$, CO_3^{2-} and HCO_3^- during 1000 years; (F) changes in species concentration of Ca^{2+} and Mg^{2+} during 1000 years; (G) changes in species concentration of $SiO_2(aq)$, K^+, Al^{3+} during 1000 years. (H) changes in species concentration of Na^+ during 1000 years.

3.4.2 Mineral reaction rates

At initial time of numerical simulations 1 and 2, the negative values of calculated saturation indices of K-feldspar, albite, quartz, and kaolinite and the positive values of calculated saturation indices of dolomite (Table 13) suggests the solution is undersaturated with respect to K-feldspar, albite, quartz, and kaolinite and saturated with respect to dolomite. At initial time of numerical simulations 3 and 4, the calculated saturation indices of K-feldspar, albite, quartz, dolomite and kaolinite are less than zero (Table 13), which indicates the solution is undersaturated with respect to K-feldspar, albite, quartz, dolomite, calcite and kaolinite. The dissolution rates of K-feldspar, albite, dolomite and calcite at initial time reached the maximum values, respectively (Table 14). With the numerical simulation proceeding, saturation indices and mineral reaction rates of all minerals decreased constantly and remained unchanged after 900 years (Fig. 8). The dissolution rate of albite in numerical simulations 1, 2 increased first and then decreased within 1000 years. The dissolution rate of albite in numerical simulations 3 decreased within 1000 years. The dissolution rate of albite in numerical simulations 4 increased first and then decreased within 500 years, and kept basically unchanged after 500 years (Fig.8C).

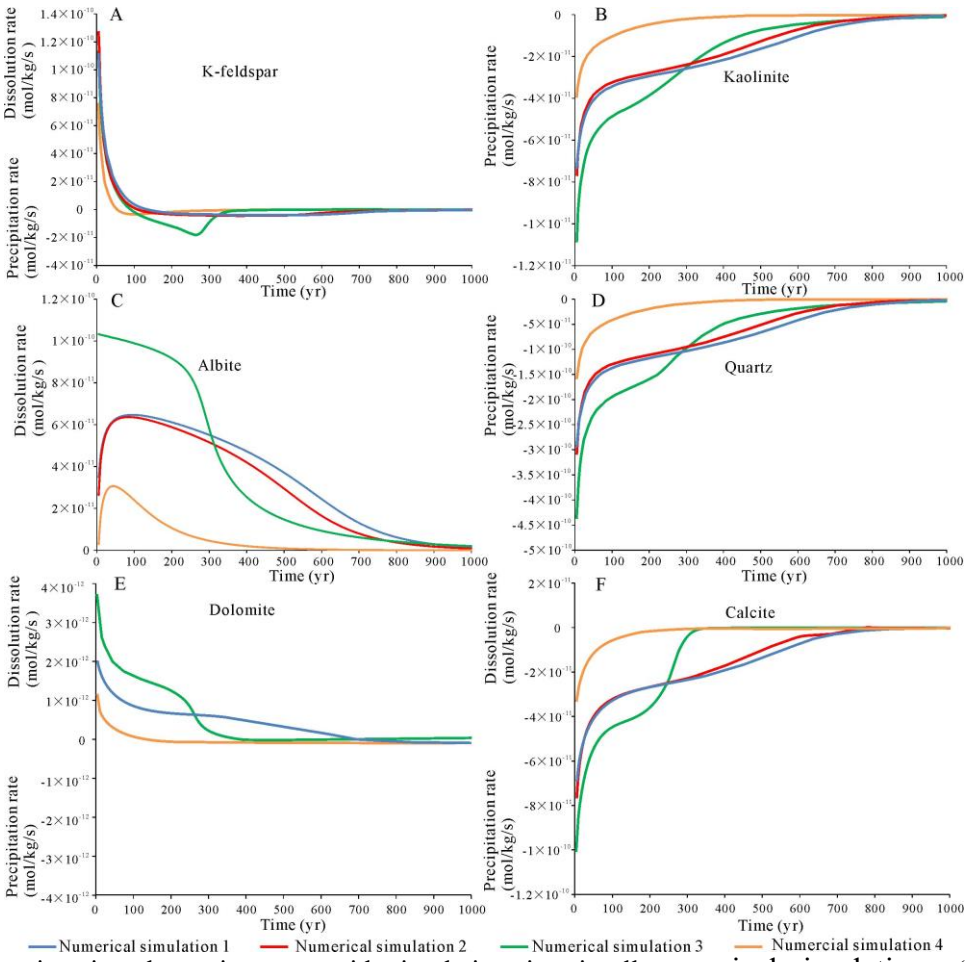

Fig. 8. Changes in mineral reaction rates with simulation time in all numerical simulations. (A) changes in mineral reaction rates of K-feldspar with simulation time; (B) changes in mineral reaction rates of kaolinite with simulation time; (C) changes in mineral reaction rates of albite with simulation time; (D) changes in mineral reaction rates of quartz with simulation time; (E) changes in mineral reaction rates of dolomite with simulation time. (F) Changes in mineral reaction rates of calcite with simulation time.

3.4.3 Change in mineralogy

The dissolved minerals were mainly K-feldspar, dolomite and albite and the newly precipitated minerals were mainly calcite, quartz and kaolinite at the initial reaction stage in all numerical simulations (Fig.9; Table 15). The dissolution mass of K-feldspar, albite and dolomite and the precipitation mass of calcite, quartz and kaolinite increased gradually with the increase of simulation time (Fig.9; Table 15). The dissolution of albite and precipitation of kaolinite and quartz reached equilibrium within 1000 years and their resulting dissolution and precipitation mass reached the maximum (Fig.9; Table 15). The dissolution of K-feldspar reached equilibrium within 200 years and their dissolution mass reached the maximum. The precipitation of calcite reached equilibrium and precipitation mass reached the maximum within 260 years in numerical simulations 3, 600 years in NS2 and 700 years in numerical simulations 4 (Fig.9F; Table 15).

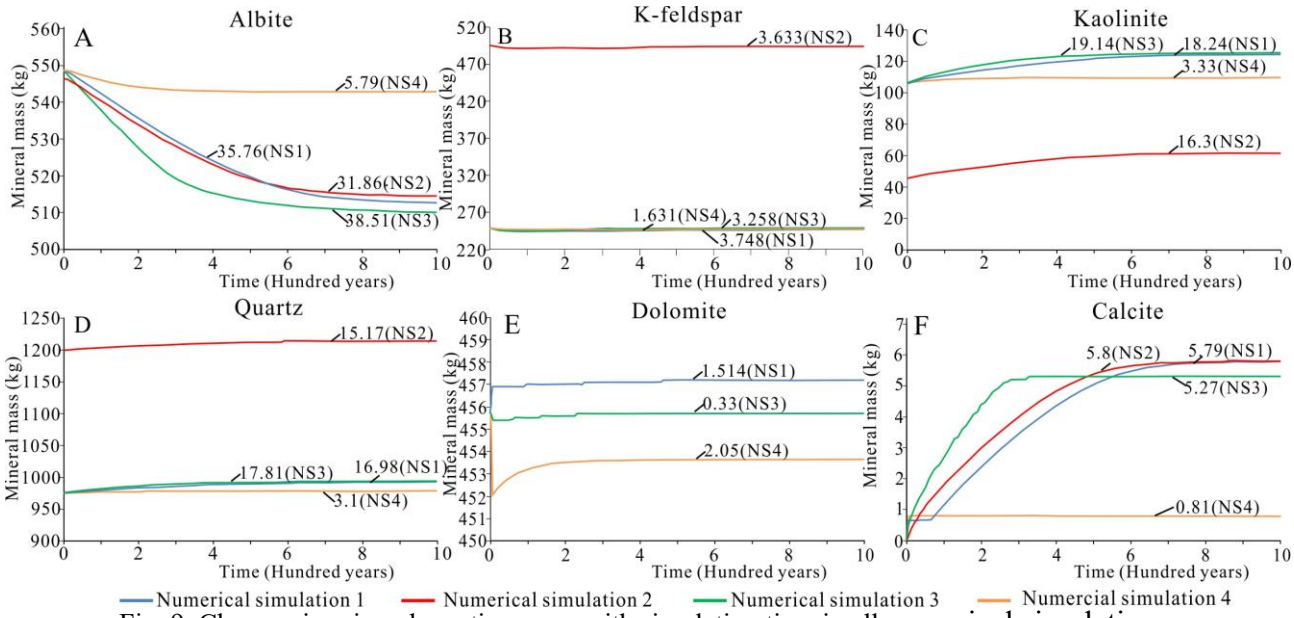

Fig. 9. Changes in mineral reaction mass with simulation time in all numerical simulations.

3.4.4 Geologic CO_2 storage

The mass of geologic CO_2 storage by solubility trapping calculated by the concentration of HCO_3^-, CO_3^{2-}, CO_2(aq) and mineral trapping increased with the increase of simulation time in all numerical simulations(Fig. 10 A). At the initial time of CO_2 injection, Geologic CO_2 storage in the sandstones rich in K-feldspar and albite with $CaCl_2$-rich formation water was controlled by solubility trapping (Fig. 10 A, B). Geologic CO_2 storage by solubility trapping was mainly in form of CO_2 (aq). As CO_2 continued to charge, the proportion of mineral trapping increased and the proportion of solubility trapping gradually decreased with the increase of reaction time (Fig. 10 B). After 900 years, the reaction of CO_2-saturated solution and the sandstones rich in K-feldspar and albite reached basically equilibrium and the geologic CO_2 storage reached the maximum (Fig. 10 A; Table 16).

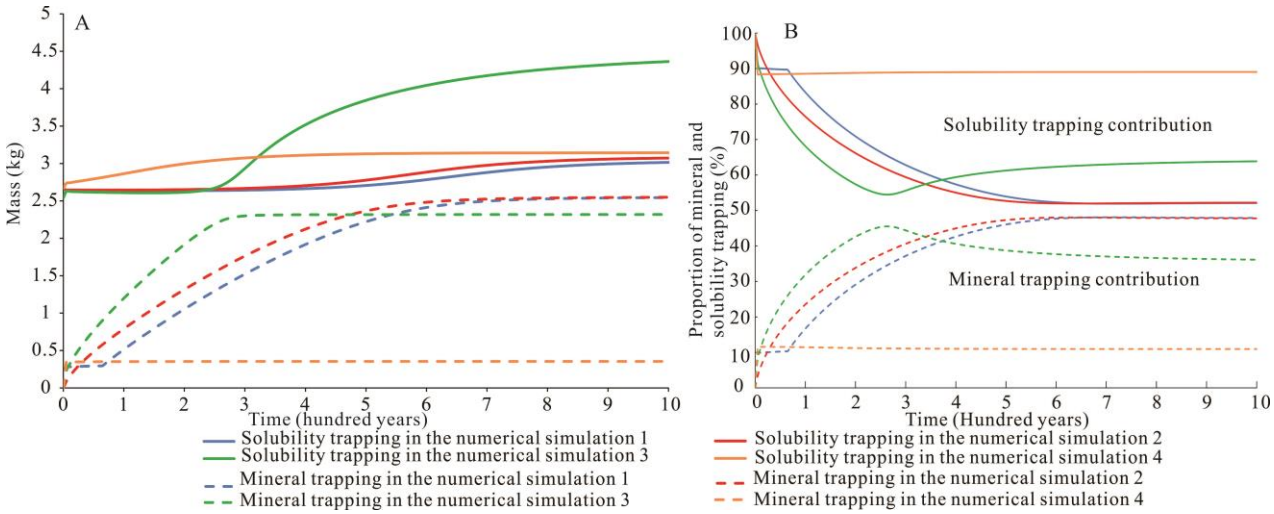

Fig. 10. Change of geologic CO_2 storage mass (A), Proportion of mineral trapping and solubility trapping (B) in the numerical simulations within 1000 years.

4. Discussion

4.1 Reaction processes of CO_2-saturated solution and sandstones rich in K-feldspar and albite

Based on mineralogy of post-experiment sandstone samples and fluid chemical composition of post-experiment solution from the short-term laboratory experiments (Figs. 3-6; Table 10), the reaction processes of CO_2-saturated solution and sandstones rich in k-feldspar and albite were proposed.

Under acidic conditions, the calculated final saturation indices of dolomite, albite and K-feldspar were negative in all the laboratory experiments (Table 11), indicating that dolomite, albite and K-feldspar were all dissolving (Figs. 3 and 4).

Dissolution of K-feldspar and albite consumed H^+ and released SiO_2, K^+ and Na^+ into solution. The final concentrations of SiO_2, K^+ and Na^+ increased significantly relative to their initial concentrations, while the final concentration of H^+ decreased in all laboratory experiments (Table 10).

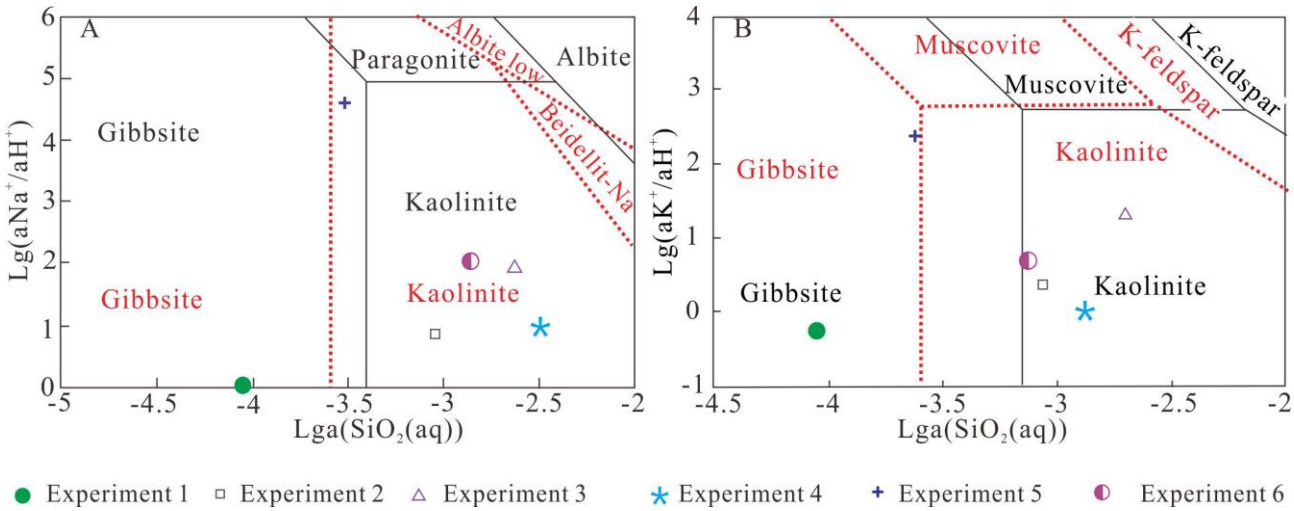

Fig. 11. Mineral activity diagram at different temperatures. (A) The paths of the radio of Si to (K^++Na^+) and pH in the post-experiment solution taken from Tutolo et al., 2015. (B) Activity diagram taken from Tutolo et al., 2015 and Choi et al., 2014 for the Na_2O-Al_2O_3-SiO_2-H_2O-CO_2 system at 100℃ (red dashed lines and red texts) and 150℃ (black solid lines and black texts). (C) Activity diagram taken from Choi et al., 2014 and Tutolo et al., 2015 for the K_2O-Al_2O_3-SiO_2-H_2O-CO_2 system at 100 ℃ (red dashed lines and red texts) and 150℃ (black solid lines and black texts).

The whole CO_2-saturated solution-aluminosilicate reaction can be divided into two stages. Firstly, K-feldspar and albite dissolution is in the stability field of gibbsite (Fig. 11 A and B). Secondly, compositional changes in solution progressed slowly toward the stability field of kaolinite (Fig. 11 A and B). The mineral phase diagram (Fig. 11 A and B) and saturation indices of authigenic minerals revealed by Laboratory experiments 4 and 6 (Table 11) provided evidences for gibbsite conversion to kaolinite. Calcite precipitation was consistent with the positive saturation indices in Laboratory experiments 3, 5 and 6 (Table 11).

In summary, during the reaction processes of CO_2-saturated solution and sandstones rich in K-feldspar and albite at 100-150°C, P_{CO2} of 4MPa, for 2 to 4 days, calcite was precipitated and dissolution of k-feldspar and albite and kaolinite precipitation also occurred simultaneously.

4.2 Mineral trapping of CO_2 in arkosic sandstones with $CaCl_2$-rich formation water

Little morphological evidence was found for the calcite precipitation in the laboratory experiment 4 for 4 days and laboratory experiment 1 with DW for 2 days, whereas calcite was precipitated in the numerical simulations for 1000 years (Fig. 9 F). Carbonate precipitation often occurred in the longer term experiments, such as experiments with CO_2-saturated, Ca^{2+}-rich solution and sandstones rich in quartz and clay minerals at 95 °C, PCO_2 of 10 MPa for 2 months (Carroll et al., 2011), CO_2-spring water-basalt at 75°C to 250°C, P_{CO2} of 11 and 24 bar for 150 days (Gysi and Stefánsson, 2012b), sandstones rich in oligoclase and solution rich in Ca^{2+} and Mg^{2+} at 200 °C and P_{CO2} of 20 MPa for 2.5 months (Kaszuba et al., 2003). Hangx and Spiers (2009) proposed that carbonates would ultimately be precipitated, given enough time for sufficient suitable ions, such as Ca^{2+}, to be liberated by dissolution of minerals rich in calcium. Therefore, non-precipitation of calcite in the laboratory experiments was probably caused by the short reaction time.

The small amount of calcite precipitation was typically much less than the original volume of the dolomite cements in Laboratory experiments 2 and 3 (Figs. 6 A, B, C). The authigenic calcites in Laboratory experiments 2 and 3 were interpreted as re-precipitation of previously dissolved dolomite cements (Figs. 4 B, C), with no net gain in CO_2 storage via mineral trapping, because the original solution was DW without Ca^{2+}. The sandstone samples in numerical simulation 1 contains a large amount of dolomite, whereas the sandstone samples in numerical simulation 2 contains no dolomite (Table 5). The mass of calcite from re-precipitation of previously dissolved dolomite cements is 0.01kg (Table 15). The total geologic CO_2 storage capability in numerical simulation 1 and 2 was similar (Table 16). Therefore, it was suggested that the dolomite content in sandstones had no effect on the geologic CO_2 storage capability. It is expected that mineral trapping via carbonate precipitation would be more effective if sufficiently dissolved Ca^{2+} is available in formation water.

Dissolution of K-feldspar and albite and precipitation of calcite were widespread and usually occurred together in the Laboratory experiments 2, 3, 5, 6 (Figs. 3 and 6) and all numerical simulation

(Fig. 8 A, C, F; Fig. 9 A, B, F). The dissolution of K-feldspar and albite was positively correlated with calcite precipitation in laboratory experiments. For example, K-feldspar and albite were dissolved more strongly in Laboratory experiments 4 and 6 (Fig. 3) than that in laboratory experiment 3, and the calcite precipitation was also more common in Laboratory experiments 4 and 6 than in laboratory experiment 3 (Fig. 6). Both the dissolution mass of K-feldspar and albite and precipitation mass of calcite increased simultaneously with the numerical simulation time (Fig. 9 A, B and F). The above correlation between dissolution of K-feldspar and albite and calcite precipitation showed that dissolution of K-feldspar and albite promoted calcite precipitation (Fig. 8A, C, F; Fig. 9 A, B, F). The dissolution of K-feldspar and albite would reduce the acidity of solution by consuming H^+ with the increase of numerical simulation time, resulting in promotion of the activity of HCO_3^-. The increase of HCO_3^- activity leaded to more calcite precipitation (Table 15) and the decrease in Ca^{2+} activity. In theory, if the H^+ from the ionization of H_2CO_3 is not consumed, $CaCl_2$ and HCO_3^- cannot react to form calcite precipitation, because H^+ will react with Cl^- to form HCl. However, calcites could be precipitated by combination of the Ca^{2+} from formation water and the CO_3^{2-} from the ionization of H_2CO_3 because the H^+ from the ionization of H_2CO_3 was consumed by dissolution of K-feldspar and albite. Many similar observations in buried sandstones showed that dissolution of K-feldspar and albite and carbonate precipitation occurred together (Armitage et al., 2010; Baker et al., 2000; Ceriani et al., 2002; Dos Anjos et al., 2000; Tobin et al., 2010; Macquaker et al., 2014; Turchyn and DePaolo , 2011; Yuan et al, 2015a, 2015b, 2015c; Zheng et al., 2015).

In the real subsurface geological environment, the dissolution of K-feldspar and albite is a very slow and continuous process with a reaction rate of $1\times10^{-14.5}$-1×10^{-22} mol/cm^2/s (Gonnenthal and Spyoher, 2001; Harouiya and Oelkers, 2004; Palandri and Kharaka, 2004; Xu el al, 2005; Kampman et al., 2009), while calcite precipitation is a rapid reaction (Arvidson et al., 2003; Kampman et al., 2009; Pokrovsky et al., 2009). K-feldspar and albite were dissolved at a slow dissolution rate (Table 14; Fig. 8 A and C) and calcite was precipitated simultaneously at a rapid precipitation rate in the numerical simulation 3 within 300 years (Fig. 8 A; Fig. 9 F). If dissolution of K-feldspar and albite does not occur in closed systems, calcite precipitation will soon reach equilibrium in a short time due to the rapid precipitation rate of calcite. However, calcite continued to precipitate with the continuous dissolution of K-feldspar and albite at the slow dissolution rate within 300 years, resulting in an increasing amount of calcite precipitation with simulation time in numerical simulation 3 (Fig. 9 F). Therefore, continuous dissolution of K-feldspar and albite at a slow rate over a long time can prolong duration time of calcite precipitation and increase geologic CO_2 storage by mineral trapping.

The concentrations of K^+, Na^+, Mg^{2+}, HCO_3^- were the same in numerical simulation 1 and 4, whereas the concentration of $CaCl_2$ in numerical simulation 1 was greater than that in numerical simulation 4 (Tables. 4 and 6; Fig. 7). The increase of Ca^+ reduced the activity of CO_3^{2-} and improved

the precipitation rate of calcite (Fig. 8 F) after 450 years, resulting in the increase of calcite precipitation mass (Table 15) and the mass of mineral trapping of CO_2 (Table 16). The precipitation mass of calcite in numerical simulation 1 was much more than that in numerical simulation 4 (Table 15). The mass of mineral trapping of CO_2 in numerical simulation 1 is much greater than that in numerical simulation 4 (Table 16). Therefore, the higher concentration of $CaCl_2$ in solution could provide source of Ca^{2+} for calcite precipitation and significantly enhance the geologic CO_2 storage capacity by mineral trapping.

The concentration of $CaCl_2$ was the same in numerical simulation 1 and 3, whereas the ions of K^+, Na^+, Mg^{2+} were not added into the original solution in numerical simulation 3 (Tables 4 and 6). The precipitation mass of calcite in numerical simulation 1 was much more than that in numerical simulation 3 (Table 15). The mass of mineral trapping of CO_2 in numerical simulation 1 was much more than that in numerical simulation 3 (Table 16). The increase of Na^+, K^+ and Mg^{2+} reduced the activity of CO_3^{2-} and improved the precipitation rate of calcite from 300 to 800 years (Fig. 8 F), resulting in the increase of calcite precipitation mass (Table 15) and the mass of mineral trapping of CO_2 (Table 16). Therefore, the increase of NaCl, KCl and $MgCl_2$ would improve the geologic CO_2 storage capacity by mineral trapping.

4.3 Processes of long-term geologic CO_2 storage

Based on the precipitation rate of calcite and the proportion of mineral trapping and solubility trapping, the long-term geologic CO_2 storage processes in the sandstones rich in K-feldspar and albite with $CaCl_2$-rich formation water can be divided into three stages (Fig. 12).

Stage I: Geologic CO_2 storage dominated by solubility trapping

This stage lasts appropriately 100 years (Fig. 12). In the initial stage, CO_2 was dissolved in formation water. The initial formation water became acidic. The dissolution of K-feldspar and albite dominated the geochemical interactions, which caused an increase of the pH value of formation water. K-feldspar and albite were dissolved at slow dissolution rate by the acidic solution and calcite was precipitated at a rapid rate within 100 years (Table 14; Fig. 8 A, C, F). Meanwhile, the precipitation rate of calcite decreased rapidly from 0 year to 100 years (Fig. 8 F). A small amount of calcite was precipitated and the mass of geologic CO_2 storage by mineral trapping is small within 100 years. The mass of calcite precipitation is 1.17kg in the numerical simulation 1 and 2.72kg in numerical simulation 3 within 100 years (Fig. 9 F). The mass of geologic CO_2 storage by mineral trapping is 0.51kg in the numerical simulation 1 and 1.2kg in numerical simulation 3 within 100 years (Fig. 12 A). Ionic activity of $CO_2(aq)$, CO_3^{2-} and HCO_3^- increased sharply, leading to a significant increase of the concentrations of $CO_2(aq)$, CO_3^{2-} and HCO_3^- (Fig. 7 E). The mass of geologic CO_2 storage capability by solubility trapping is large in the stage I. The mass of geologic CO_2 storage by solubility trapping is 2.64kg in the numerical simulation 1 and 2.61kg in numerical simulation 3 within 100

years (Fig. 12 A). The proportion of solubility trapping decreased and the proportion of mineral trapping increased in the stage I. The proportion of solubility trapping was larger than that of mineral trapping within 100 years (Fig. 12 B). Therefore, CO_2 in stage I is dominantly stored as CO_2(aq), CO_3^{2-} and HCO_3^- by solubility trapping with small amounts of carbonate precipitation.

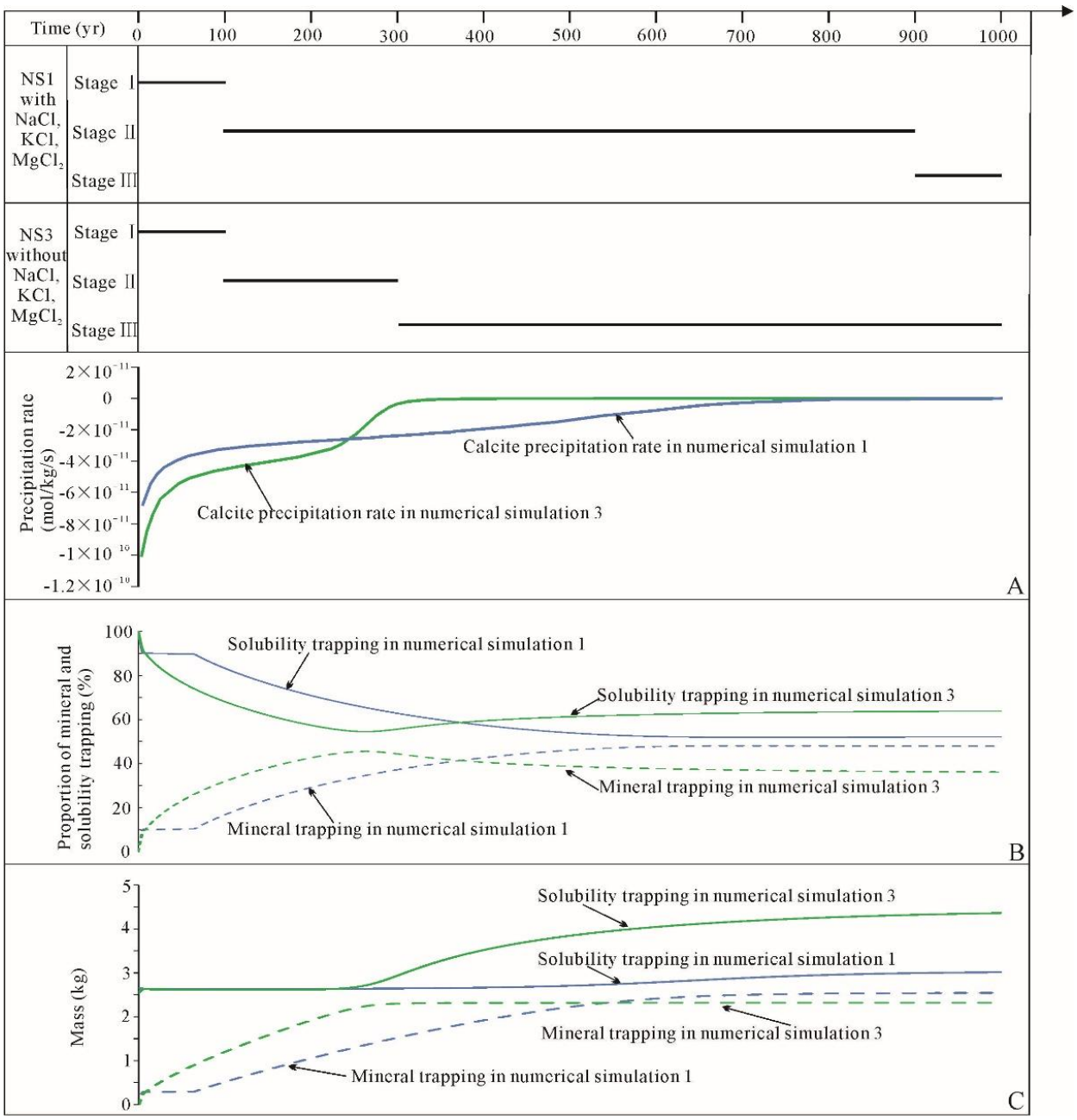

Fig. 12. Stage classification of the long-term geologic CO_2 storage processes. (A) Changes of calcite precipitation rate; (B) Proportion of solubility trapping and mineral trapping; (C) Mass changes of geologic CO_2 storage by solubility trapping and mineral trapping.

Stage II: Geologic CO_2 storage dominated by mineral trapping

In the solution without NaCl, KCl and $MgCl_2$, this stage lasted approximately from 100 years to 300 years. The pH of solution continued to increase to the maximum value of 6, because the dissolution of albite and K-feldspar consumed a large amount of H^+. The precipitation rate of calcite decreased abruptly and reached the equilibrium within 300 years (Fig. 8F). The precipitation mass of

calcite and the mass of geologic CO_2 storage by mineral trapping increased from 100 years to 300 years (Fig. 12A). The mass of calcite precipitation is 5.27kg (Fig. 9 F) and the mass of geologic CO_2 storage by mineral trapping is 2.3kg within 300 years in numerical simulation 3 (Fig. 12 A). The proportion of mineral trapping increased from 100 years to 300 years and reached to 40% in 300 years (Fig. 12 B).

In the solution with the addition of NaCl, KCl and $MgCl_2$, the duration of stage II prolonged to 900 years. The precipitation rate of calcite decreased slowly from 100 years to 900 years (Fig 8 F). The duration time of K-feldspar and albite and calcite precipitation prolonged to 900 years, and the precipitation mass of calcite (Fig 9 F) and the mass of geologic CO_2 storage by mineral trapping increased from 100 years to 900 years (Fig 12 A). The mass of calcite precipitation increased to 5.79 kg in the numerical simulation 1 within 900 years (Fig. 9 F). The mass of geologic CO_2 storage by mineral trapping is 2.48kg in the numerical simulation 1 (Fig. 12 A). The proportion of mineral trapping increased from 100 years to 900 years and reached 47% in numerical simulation 1.

Stage III (900 years-): Interaction in Equilibrium

With the increase of CO_2 charging time, the system of K-feldspar, albite, dolomite and calcite reacting with CO_2-saturated solution reached equilibrium (Figs. 8 and 9). The geologic CO_2 storage reached the maximum capacity (Fig. 12 B and C), but the final proportion of mineral trapping of CO_2 is still less than 50%.

4.4 Long-term geologic CO_2 storage capability

The results of long-term numerical simulation lasting 10000 years showed that it is feasible to inject CO_2 into the depleted oil and gas reservoirs at 150°C and P_{CO2} of 4MPa in the Es4x to Es3z in the Dongying Sag. The Ca^{2+} in the formation water with the concentration of 0.38mol/L is a major calcium source. The geologic CO_2 storage capacity calculated by numerical simulation 5 is about 7.18 kg/m^3 by solubility trapping and about 4.95 kg/m^3 by mineral trapping (Table 16). The volume of the sandstones reservoirs of the Es4x to Es3z at depth interval from 2200m to 3300m calculated by Zhang et al (2007) is $7.305\times10^{11}m^3$. Based on the result of numerical simulation lasting 10000 years and the calculated volume of the sandstones reservoirs, the calculated total geologic CO_2 storage capacity by solubility trapping and mineral trapping is about 5.24GT and 3.61GT, respectively.

5. Conclusions

$CaCl_2$ in formation water can be an important calcium source for mineral trapping of CO_2 in the sandstones rich in K-feldspar and albite without calcium-containing minerals, because dissolution of K-feldspar and albite reduce the acidity of solution by consuming H^+ in long-term processes of geologic CO_2 storage. The continuous dissolution of K-feldspar and albite at a slow rate within a long time can prolong duration time of calcite precipitation and increase the geologic CO_2 storage capability by mineral trapping. Addition of NaCl, KCl and $MgCl_2$ into the CO_2-saturated solution

could increase mineral trapping of CO_2 and total geologic CO_2 storage capability. The depleted oil and gas fields with the sandstones rich in feldspar and albite and formation water rich in $CaCl_2$ are favorable sites for long-term stable geologic CO_2 storage.

Long-term geologic CO_2 storage processes in the sandstones rich in feldspar and albite and $CaCl_2$-rich formation water can be divided into three stages. In stage I, geologic CO_2 storage is dominated by solubility trapping within 100 years. In stage II, geologic CO_2 storage is dominated by mineral trapping from 100 years to 300 years without NaCl, KCl and $MgCl_2$, or to 900 years with addition of NaCl, KCl and $MgCl_2$. In stage III, the reactions between CO_2-saturated solution and the sandstones rich in K-feldspar and albite reached equilibrium.

Acknowledgements

This study was supported by the National Natural Science Foundation of China (41772137, 41602138，41872140), the National Science and Technology Special Grant (2016ZX05006-003-003; 2016ZX05006-007), and the Fundamental Research Funds for the Central Universities (17CX05009). We would like to thank Exploration and Development Research Institute, Shengli Oilfield, Sinopec, China, for providing core samples and porosity and permeability data.

Reference

Aagaard, P. & Helgeson, H.C. (1982) Thermodynamic and kinetic constraints on reaction rates among minerals and aqueous solutions. I Theoretical considerations. American J. Science V.282, 237-285.

Alia, B G., Emmanuelle, C., Louis-César, P., Jean-François Blais and Guy Mercier. (2015) CO2 sequestration using waste concrete and anorthosite tailings by direct mineral carbonation in gas-solid-liquid and gas-solid routes. Journal of Environmental Management, 163:70.

Aradóttir, E.S.P., Hólmfrídur Sigurdardóttir., Bergur Sigfússon and Einar Gunnlaugsson. (2011). Carbfix: a CCS pilot project imitating and accelerating natural CO2 sequestration. Greenhouse Gases Science & Technology, 1 (2), 105-118.

Armitage, P. J., Worden, R. H., Faulkner, D. R, Aplin, A. C., Butcher, A. R. and Iliffe, J. (2010). Diagenetic and sedimentary controls on porosity in lower carboniferous fine-grained lithologies, krechba field, algeria: a petrological study of a caprock to a carbon capture site. Marine and Petroleum Geology, 27 (7), 0-1410.

Arvidson, R. S., Ertan, I. E., Amonette, J. E. and Luttge, A. (2003). Variation in calcite dissolution rates: A fundamental problem?. Geochimica et Cosmochimica acta, 67 (9), 1623-1634.

Bachu, S., Bonijoly, D., Bradshaw, J., Burruss, R., Holloway, S., Christensen, N. P. and Mathiassen, O. M. (2007). CO2 storage capacity estimation: Methodology and gaps. Int. J. Greenh. Gas Control, 1 (4), 430-443.

Baker, J. C., Havord, P. J., Martin, K. R. and Ghori, K. A. R. (2000). Diagenesis and petrophysics of the Early Permian Moogooloo sandstone, southern Carnarvon basin, western Australia. AAPG bulletin, 84 (2), 250-265.

Cao, Y. C., Wang, Y. Z., Gluyas, J. G., Liu, H. and Song, M. S. (2018). Depositional model for lacustrine nearshore subaqueous fans in a rift basin: The Eocene Shahejie Formation, Dongying Sag, Bohai Bay Basin, China. Sedimentology, 65 (6), 2117-2148.

Cao, Y. C., Yuan, G. H., Li, X. Y., Wang, Y. Z, Xi, K. L., Wang, X. M., Jia, Z. Z. and Yang, T. (2014). Characteristics and origin of abnormally high porosity zones in buried Paleogene clastic reservoirs in the Shengtuo area, Dongying Sag, East China. Petroleum Science, 11 (3), 346-362.

Carroll, S. A., Mcnab, W. W. and Torres, S. C. (2011). Experimental study of cement - sandstone/shale - brine - CO2 interactions. Geochemical Transactions, 12 (1), 9-9.

Celia, M. A. and Nordbotten, J. M. (2009). Practical modeling approaches for geological storage of carbon dioxide. Groundwater, 47 (5), 627-638.

Ceriani, A., Di, G. A., Goldstein, R. H. and Rossi, C. (2002). Diagenesis associated with cooling during burial: An example from Lower Cretaceous reservoir sandstones (Sirt Basin, Libya). AAPG bulletin, 86 (9), 1573-1591.

Choi, B. Y., Yun, S. T., Kim, K. H., Choi, H. S., Chae, G. T. and Lee, P. K. (2014). Geochemical modeling of CO2-water-rock interactions for two different hydrochemical types of CO_2-rich springs in Kangwon District, Korea. Journal of Geochemical Exploration, 144, 49-62.

De Coninck H, Benson S M. Carbon dioxide capture and storage: issues and prospects[J]. Annual review of environment and resources, 2014, 39: 243-270.

Dos Anjos, S. M., De Ros, L. F., De Souza, R. S., De Assis Silva, C. M. and Sombra, C. L. (2000). Depositional and diagenetic controls on the reservoir quality of Lower Cretaceous Pendencia sandstones, Potiguar rift basin, Brazil. AAPG bulletin, 84 (11), 1719-1742.

Elmabrouk, S. K., Bader, H. E. and Mahmud, W M. (2017). An Overview of Power Plant CCS and CO2-EOR Projects. International Conference on Industrial Engineering and Operations Management.

Fischer, S., Zemke, K., Liebscher, A. and Wandrey, M. and CO2 SINK Group. (2011). Petrophysical and petrochemical effects of long-term CO2-exposure experiments on brine-saturated reservoir sandstone. Energy Procedia, 4, 4487-4494.

Fu, Q., Lu, P., Konishi, H., Dilmore, R., Xu, H., Seyfried Jr, W. E. and Zhu, C. (2009). Coupled alkali-feldspar dissolution and secondary mineral precipitation in batch systems: 1. New experiments at 200°C and 300 bars. Chemical Geology, 258 (3-4), 125-135.

Gaus, I. (2010). Role and impact of CO2-rock interactions during CO2 storage in sedimentary rocks. Int. J. Greenh. Gas Control, 4 (1), 73-89.

Gilfillan, S. M., Lollar, B. S., Holland, G., Blagburn, D., Stevens, S., Schoell, M. and Ballentine, C. J. (2009). Solubility trapping in formation water as dominant CO2 sink in natural gas fields. Nature, 458 (7238), 614.

Gluyas, J.G. and Mathias, S.A. (2013) Geological storage of carbon dioxide (CO2), Geoscience, technologies, environmental aspects and legal frameworks, Woodhead Publishers ISBN 978-0-85709-427-8 (Print) 978-0-85709-727-9 (Online)

Gunter, W.D., Wiwchar, B. & Perkins, E.H. (1997) Aquifer disposal of CO2-rich greenhouse gases: extension of time scale of experiment of CO2-sequestering reactions by geochemical modeling. Mineralogy Petrology v.59, 121-140

Sundal, A. & Hellevang, H. (2019) Using Reservoir Geology and Petrographic Observations to Improve CO2 Mineralization Estimates: Examples from the Johansen Formation, North Sea, Norway Minerals 2019, 9, 671

Gunter, W. D., Perkins, E. H. and Hutcheon, I. (2000). Aquifer disposal of acid gases: modelling of water-rock reactions for trapping of acid wastes. Applied Geochemistry, 15 (8), 1085-1095.

Guo, X., Liu, K., He, S., Song, G., Wang, Y., Hao, X. and Wang, B. (2012). Petroleum generation and charge history of the northern Dongying Depression, Bohai Bay Basin, China: insight from integrated fluid inclusion analysis and basin modelling. Marine and Petroleum Geology, 32 (1), 21-35.

Gysi, A. P. and Stefánsson, A. (2011) CO2-water-basalt interaction. Numerical simulation of low temperature CO2 sequestration into basalts. Geochimica et Cosmochimica Acta, 75 (17): 4728-4751.

Gysi, A. P. and Stefánsson, A. (2012a). Experiments and geochemical modeling of CO2 sequestration during hydrothermal basalt alteration. Chemical Geology, 306, 10-28.

Gysi, A. P. and Stefánsson, A. (2012b). Mineralogical aspects of CO2 sequestration during hydrothermal basalt alteration—an experimental study at 75 to 250°C and elevated PCO2. Chemical Geology, 306, 146-159.

Hangx, S. J. and Spiers, C. J. (2009). Reaction of plagioclase feldspars with CO2 under hydrothermal conditions. Chemical Geology, 265 (1-2), 88-98.

He S., Lv, L., Liang, B., Li, C., Yuan, B., Ye, L. and Xie, H. (2015). Aqueous carbonation of the potassium-depleted residue from potassium feldspar–CaCl2 calcination for CO2 fixation. Environmental Earth Sciences, 73 (11), 6871-6879.

Hellevang, H., Miri, R. and Haile, B. G. (2014). New Insights into the mechanisms controlling the rate of crystal growth. Crystal Growth & Design, 14 (12), 6451-6458.

Hitchon, B., Gunter, W. D., Gentzis, T. and Bailey, R. T. (1999). Sedimentary basins and greenhouse gases: a serendipitous association. Energy Conversion and Management, 40 (8), 825-843.

Jackson, R. B., Le Quéré, C., Andrew, R. M., Canadell, J. G., Peters, G. P., Roy, J. and Wu, L. (2017). Warning signs for stabilizing global CO2 emissions. Environmental Research Letters, 12 (11), 110202.

Jenkins C R, Cook P J, Ennis-King J, et al. Safe storage and effective monitoring of CO_2 in depleted gas fields[J]. Proceedings of the National Academy of Sciences, 2012, 109(2): E35-E41.

Kampman, N., Bickle, M., Becker, J., Assayag, N. and Chapman, H., 2009. Feldspar dissolution kinetics and Gibbs free energy dependence in a CO2-enriched groundwater system, Green River, Utah. Earth Planet. Sci. Lett. 284 (3-4), 473-488.

Kaszuba, J. P., Janecky, D. R. and Snow, M. G. (2003). Carbon dioxide reaction processes in a model brine aquifer at 200°C and 200 bars: implications for geologic sequestration of carbon. Applied Geochemistry, 18 (7), 1065-1080.

Kirsch, K., Navarre-Sitchler, A. K., Wunsch, A. and McCray, J. E. (2014). Metal release from sandstones under experimentally and numerically simulated CO2 leakage conditions. Environmental Science & Technology, 48 (3), 1436-1442.

Klett, T. R., Ahlbrandt, T. S., Schmoker, J. W. and Dolton, G. L. (1997). Ranking of the world's oil and gas provinces by known petroleum volumes. Center for Integrated Data Analytics Wisconsin Science Center.

Kumar, A., Shrivastava, J. P. and Pathak, V. (2017). Mineral carbonation reactions under water-saturated, hydrothermal-like conditions and numerical simulations of CO2 sequestration in tholeiitic basalt of the eastern deccan volcanic province, india. Applied Geochemistry, 84.

Lasaga, A. C.(1981) Rate laws of chemical reactions, in Kinetics of Geochemical Processes, Rev. Mineral., vol. 8 edited by A. C. Lasaga and R. J. Kirkpatrick, pp. 1-67, Mineralogical Society of America, Washington,D.C., 1981.

Lee, M. R. and Parsons, I. (1995). Microtextural controls of weathering of perthitic alkali feldspars. Geochimica et Cosmochimica Acta, 59 (21), 4465-4488.

Leung, D. Y. C., Caramanna, G. and Marotovaler, M. M. (2014). An overview of current status of carbon dioxide capture and storage technologies. Renewable & Sustainable Energy Reviews, 39 (39), 426-443.

Li, D. and Duan, Z. (2007). The speciation equilibrium coupling with phase equilibrium in the H2O-CO2-NaCl system from 0 to 250°C, from 0 to 1000 bar, and from 0 to 5 molality of NaCl. Chemical Geology, 244 (3-4), 730-751.

Li, F., Cao, Y., Li, W. and Zhang, L. (2018). CO2 mineral trapping: Hydrothermal experimental assessments on the thermodynamic stability of dawsonite at 4.3 Mpa PCO2 and elevated temperatures. Greenhouse Gases: Science and Technology, 8 (1), 77-92.

Li, X., Wei, N., Liu, Y., Fang, Z., Dahowski, R. T. and Davidson, C. L. (2009). CO2 point emission and geological storage capacity in China. Energy Procedia, 1 (1), 2793-2800.

Li, Y. and Pang, Z. (2016). Capacity and suitability assessment of deep saline aquifers for CO2 sequestration in the Bohai Bay Basin, East China. Environmental Earth Sciences, 75 (5), 402.

Li, Y., and Pang, Z. (2017). Hydrogeochemical characteristics of deep saline aquifers in sedimentary basins in China and implications for CO2 geological storage with emphasis on total dissolved solids (TDS) and water type. Greenhouse Gases: Science and Technology, 7 (1), 53-64.

Liu, B., Yang, Y., Li, Jiangtao, Chi, Y., Li, Junhui, Fu, X., 2020. Stress sensitivity of tight reservoirs and its effect on oil saturation: A case study of Lower Cretaceous tight clastic reservoirs in the Hailar Basin, Northeast China. Journal of Petroleum Science and Engineering 184, 106484.

Liu, N., Liu, L., Qu, X., Yang, H., Wang, L. and Zhao, S. (2011). Genesis of authigene carbonate minerals in the Upper Cretaceous reservoir, Honggang Anticline, Songliao Basin: A natural analog for mineral trapping of natural CO2 storage. Sedimentary Geology, 237 (3-4), 166-178.

Lu, J., Mickler, P. J., Nicot, J. P., Yang, C. and Romanak, K. D. (2014). Geochemical impact of oxygen on siliciclastic carbon storage reservoirs. Int. J. Greenh. Gas Control, 21, 214-231.

Lu, J., Partin, J. W., Hovorka, S. D. and Wong, C. (2010). Potential risks to freshwater resources as a result of leakage from CO2 geological storage: a batch-reaction experiment. Environmental Earth Sciences, 60 (2), 335-348.

Luhmann, A. J., Kong, X. Z., Tutolo, B. M., Ding, K., Saar, M. O. and Seyfried Jr, W. E. (2012). Permeability reduction produced by grain reorganization and accumulation of exsolved CO2 during geologic carbon sequestration: A new CO2 trapping mechanism. Environmental Science & Technology, 47 (1), 242-251.

Luquot, L., Andreani, M., Gouze, P. and Camps, P. (2012). CO2 percolation experiment through chlorite/zeolite-rich sandstone (Pretty Hill Formation–Otway Basin–Australia). Chemical Geology, 294, 75-88.

Macquaker, J. H., Taylor, K. G., Keller, M. and Polya, D. (2014). Compositional controls on early diagenetic pathways in fine-grained sedimentary rocks: Implications for predicting unconventional reservoir attributes of mudstones Diagenesis of Organic-Rich Mudstones. AAPG bulletin, 98 (3), 587-603.

Masters, C. D., Root, D. H. and Turner, R. M. (1998). World conventional crude oil and natural gas; identified reserves, undiscovered resources and futures (No. 98-468)

Matter, J. M. and Kelemen, P. B. (2009). Permanent storage of carbon dioxide in geological reservoirs by mineral carbonation. Nature Geoscience, 2 (12), 837.

Matter, J. M., Stute, M., Snæbjörnsdottir, S. Ó., Oelkers, E. H., Gislason, S. R., Aradottir, E. S., and Axelsson, G. (2016). Rapid carbon mineralization for permanent disposal of anthropogenic carbon dioxide emissions. Science, 352 (6291), 1312-1314.

McGrail, B. P., Schaef, H. T., Ho, A. M., Chien, Y. J., Dooley, J. J. and Davidson, C. L. (2006). Potential for carbon dioxide sequestration in flood basalts. Journal of Geophysical Research: Solid Earth, 111 (B12).

Munz, I. A., Brandvoll, Ø., Haug, T. A., Iden, K., Smeets, R., Kihle, J. and Johansen, H. (2012). Mechanisms and rates of plagioclase carbonation reactions. Geochimica et Cosmochimica Acta, 77, 27-51.

Myer, L. (2011). Global status of geologic CO2 storage technology development. United States carbon sequestration council report July.

Perkins, E.H. & Gunter, W.D. (1995) Aquifer disposal of CO2-rich greenhouse gases: Modelling of water-rock reaction paths in a siliciclastic aquifer. In Kharaka, Y.K., Chudaev, O,V. (eds), Proc. 8th Internat, Symp. on Water-Rock Interaction. pp 895-898

Peters, G. P., Le, Quéré C., Andrew, R. M., Canadell, J. G., Friedlingstein, P., Ilyina, T. and Sitch, S. (2017). Towards real-time verification of CO2 emissions. Nature Climate Change, 7 (12), 848.

Pokrovsky, O. S., Golubev, S. V. and Jordan, G. (2009). Effect of organic and inorganic ligands on calcite and magnesite dissolution rates at 60°C and 30 atm PCO2. Chemical Geology, 265 (1-2), 33-43.

Raistrick, M., Hutcheon, I., Shevalier, M., Nightingale, M., Johnson, G., Taylor, S. and Gunter, B. (2009). Carbon dioxide-water-silicate mineral reactions enhance CO2 storage; evidence from produced fluid measurements and geochemical modeling at the IEA Weyburn-Midale Project. Energy Procedia, 1 (1), 3149-3155.

Scislewski, A. and Zuddas, P. (2010). Estimation of reactive mineral surface area during water-rock interaction using fluid chemical data. Geochimica et Cosmochimica Acta, 74 (24), 6996-7007.

Shukla, R., Ranjith, P., Haque, A. and Choi, X. (2010). A review of studies on CO2 sequestration and caprock integrity. Fuel, 89 (10), 2651-2664.

Stevens, S. H., Kuuskraa, V. A., Gale, J. and Beecy, D. (2001). CO_2 injection and sequestration in depleted oil and gas fields and deep coal seams: worldwide potential and costs. Environmental Geosciences, 8 (3), 200-209

Sundal, A. & Hellevang, H. (2019) Using Reservoir Geology and Petrographic Observations to Improve CO2 Mineralization Estimates: Examples from the Johansen Formation, North Sea, Norway Minerals 2019, 9, 671

Tobin, R. C., McClain, T., Lieber, R. B., Ozkan, A., Banfield, L. A., Marchand, A. M. and McRae, L. E. (2010). Reservoir quality modeling of tight-gas sands in Wamsutter field: Integration of diagenesis, petroleum systems, and production data. AAPG bulletin, 94 (8), 1229-1266.

Turchyn, A. V. and DePaolo, D. J. (2011). Calcium isotope evidence for suppression of carbonate dissolution in carbonate-bearing organic-rich sediments. Geochimica et Cosmochimica Acta, 75 (22), 7081-7098.

Tutolo, B. M., Luhmann, A. J., Kong, X. Z., Saar, M. O. and Seyfried, W. E. (2015). CO_2 sequestration in feldspar-rich sandstone: coupled evolution of fluid chemistry, mineral reaction rates, and hydrogeochemical properties. Geochimica et Cosmochimica Acta, 160, 132-154.

Van der Zwaan, B. and Smekens, K. (2009). CO2 capture and storage with leakage in an energy-climate model. Environmental Modeling & Assessment, 14 (2), 135-148.

Van Pham, T. H., Aagaard, P. and Hellevang, H. (2012). On the potential for CO2 mineral storage in continental flood basalts-phreeqc batch- and 1d diffusion-reaction simulations. Geochem Trans, 13 (1), 5.

Wang, Y. Z. (2010). Genetic mechanism and evolution model of secondary pore development zone of Paleogene in the north zone in Dongying Depression. Qingdao: China University of Petroleum (Huadong). (in Chinese with English abstract)

Wigand, M., Carey, J. W., Schütt, H., Spangenberg, E. and Erzinger, J. (2008). Geochemical effects of CO2 sequestration in sandstones under simulated in situ conditions of deep saline aquifers. Applied Geochemistry, 23 (9), 2735-2745.

Wolff-Boenisch, D. and Galeczka, I. M. (2018). Flow-through reactor experiments on basalt-(sea) water-CO2 reactions at 90°C and neutral pH. What happens to the basalt pore space under post-injection conditions?. Int. J. Greenh. Gas Control, 68, 176-190.

Xu, T., Apps, J. A. and Pruess, K. (2004). Numerical simulation of co disposal by mineral trapping in deep aquifers. Applied Geochemistry, 19 (6), 917-936.

Yang, F., Bai, B., Tang, D., Shari, D. N. and David, W. (2010). Characteristics of CO2 sequestration in saline aquifers. Petroleum Science, 7 (1), 83-92.

Yang, L., Xu, T., Feng, G., Liu, K., Tian, H., Peng, B. and Wang, C. (2017). CO2-induced geochemical reactions in heterogeneous sandstone and potential conditions causing the tight cementation. Applied Geochemistry, 80, 14-23

Yu, Z., Liu, K., Liu, L., Yang, S. and Yang, Y. (2017). An experimental study of CO2-oil-brine-rock interaction under in situ reservoir conditions. Geochemistry, Geophysics, Geosystems, 18 (7), 2526-2542.

Yu, Z., Liu, L., Liu, K., Yang, S. and Yang, Y. (2015). Petrological characterization and reactive transport simulation of a high-water-cut oil reservoir in the Southern Songliao Basin, Eastern China for CO2 sequestration. Int. J. Greenh. Gas Control, 37, 191-212.

Yuan, G. H., Cao, Y. C, Gluyas, J., Li, X., Xi, K. L., Wang, Y. Z. and Oxtoby, N. H. (2015a). Feldspar dissolution, authigenic clays, and quartz cements in open and closed sandstone geochemical systems during diagenesis: Typical examples from two sags in Bohai Bay Basin, East China. AAPG Bulletin, 99 (11), 2121-2154.

Yuan, G. H., Cao, Y. C., Gluyas, J. and Jia, Z. Z. (2017b). Reactive transport modeling of coupled feldspar dissolution and secondary mineral precipitation and its implication for diagenetic interaction in sandstones. Geochimica et Cosmochimica Acta, 207, 232-255.

Yuan, G. H., Cao, Y. C., Gluyas, J., Cao, X. and Zhang, W. (2017a). Petrography, fluid inclusion, isotope and trace element constraints on the origin of quartz cementation and feldspar dissolution and the associated fluid evolution in arkosic sandstones. AAPG Bulletin, (20, 170,615).

Yuan, G. H., Cao, Y. C., Jia, Z. Z., Gluyas, J., Yang, T., Wang, Y. Z. and Xi, K. L. (2015b). Selective dissolution of feldspars in the presence of carbonates: The way to generate secondary pores in buried sandstones by organic CO2. Marine and Petroleum Geology, 60, 105-119.

Yuan, G. H., Gluyas, J., Cao, Y. C, Oxtoby, N. H., Jia, Z. Z., Wang, Y. Z. and Li, X. (2015c). Diagenesis and reservoir quality evolution of the Eocene sandstones in the northern Dongying Sag, Bohai Bay Basin, East China. Marine and Petroleum Geology, 62, 77-89.

Yuan, J. and Wang, Q. Z. (2001). Distribution and generation of deep reservoir secondary pores, Paleogene, Dongying Sag. Journal of Mineralogy and Petrology, 21 (1), 43-47.

Zhang Shanwen (2007). “Water Consumption” in Diagenetic Stage and Its Petroleum Geological Significance. Acta Sedimentologica Sinica, 5, 006.

Zheng, H., Feng, X. T. and Pan, P. Z. (2015). Experimental investigation of sandstone properties under CO2-NaCl solution-rock interactions. Int. J. Greenh. Gas Control, 37, 451-470.

Zhu, C. and Lu, P. (2009). Alkali feldspar dissolution and secondary mineral precipitation in batch systems: 3. Saturation states of product minerals and reaction paths. Geochimica et Cosmochimica Acta, 73 (11), 3171-3200.

Appendix 1. Tables

Table 1. Experimental conditions and processes for the laboratory experiments.

Experiments	Temperature, ℃	P_{CO2}, MPa	Reaction time, h	Reaction solution	Samples
1	100	4	48	DW	DLF-LE
2	150	4	48	DW	DLF-LE
3	150	4	96	DW	DLF-LE
4	150	4	96	SHCa-LE	FL-LE
5	150	4	96	FW-LE	DLF-LE
6	150	4	96	SHCa-LE	DLF-LE

Note：DW, deionized water. FW-LE, formation water in the laboratory experiment 5. SHCa-LE, solution with $CaCl_2$ concentration of 0.38 mol/L in the laboratory experiments 4 and 6. DLF-LE, dolomitic lithic feldsarenite in the Laboratory experiments. FL-LE, feldspathic lithirenite in the laboratory experiments.

Table 2. Ion concentration of the solution in the laboratory experiments.

Ion types	FW-LE(formation water in the laboratory experiment 5)		SHCa-LE(solution with $CaCl_2$ concentration of 0.38 mol/L in the laboratory experiments 4 and 6)	
	Concentration, mol/L	Mass, g	Concentration, mol/L	Mass, g
K^+	0.012	0.0936		
Na^+	3.72	17.112		
Ca^{2+}	0.38	3.04	0.38	3.04
Mg^{2+}	0.053	0.2544		
Cl^-	4.58	32.518	0.76	5.396

Table 3. Equilibrium constants (lg Keq) calculated by mineral dissolution reaction.

Minerals	Mineral dissolution reaction	100℃	150℃	Reference
K-feldspar	$KAlSi_3O_8+8H_2O=K^++Al(OH)_4-+3H_4SiO_4$	−18.54	−16.49	Gysi and Stefánsson, 2012a; Fischer et al., 2011
Albite	$NaAlSi_3O_8+8H_2O=Na^++Al(OH)_4^-+3H_4SiO_4$	−15.75	−14.3	Gysi and Stefánsson, 2012a; Fischer et al., 2011
Quartz	$SiO_2+2H_2O=H_4SiO_4^0$	−2.98	−2.61	Gysi and Stefansson, 2011
Kaolinite	$Al_2Si_2O_5(OH)_4+7H_2O=2Al(OH)_4^-+2H^++2H_4SiO_4$	−33.72	−30.47	Gysi and Stefansson, 2011
dolomite	$CaMg(CO_3)_2+2H^+=Ca^{2+}+Mg^{2+}+2HCO_3^-$	0.76	−0.76	Gysi and Stefansson, 2011
Calcite	$CaCO_3=Ca^{2+}+CO_3^{2-}$	−9.25	−10.05	Gysi and Stefánsson, 2012a; Fischer et al., 2011
Gibbsite	$AlO_2H +3H^+ = Al^{+3} + 2H_2O$	4.849	2.354	Zhu and Lu, 2009

Table 4. Conditions of the numerical simulations(NSS) on the reaction of CO_2-saturated solution and sandstones rich in K-feldspar and albite

NSS	Temperature,℃	P_{CO2}, MPa	Reaction time, yr	Reaction solution	Samples
1	150	4	1000	FW-NS	DLF-NS
2	150	4	1000	FW-NS	FL-NS
3	150	4	1000	SHCa-NS	DLF-NS
4	150	4	1000	SLCa-NS	DLF-NS
5	150	4	10000	FW-NS	DLF-NS1

Note: DLF-NS, dolomitic lithic feldsarenite in the numerical simulaitons which is rich in K-feldspar, albite and dolomite. FL-NS, feldsparthic lithirenite in the numerical simulaitons which is rich in K-feldspar and albite and lacks dolomite; FW-NS, formation water in the numerical simulaitons; SHCa-NS, solution with $CaCl_2$ concentration of 0.38 mol/L in the numerical simulations. SLCa-NS, solution with $CaCl_2$ concentration of 0.001 mol/L in the numerical simulaiton. See table 5 for mineral composition of DLF-NS, FL-NS and DLF-NS1. See Table 6 for the ion composition of reaction solution.

Table 5. Simplified mineral composition in the numerical simulations .

Content	NM	Minerals					
		Quartz	K-feldspar	Albite	Dolomite	Kaolinite	Porosity
Volume fraction, %	DLF-NS	36.8	9.6	20.8	15.9	4.1	12.8
	FL-NS	45.2	19.1	20.8		1.7	13.1

	DLF-NS1	31.9	18	16.9	4.6	3	25.6
Mass, kg	DLF-NS	975.46	248.55	548.57	455.69	106.33	127.6
	FL-NS	1199.29	495.16	546.43		45.36	131
	DLF-NS1	988	546	520	156	91	299

Note: Porosity of DLF-NS is the average porosity of the Es4x to Es3z sandstones in the Shengtuo area. Porosity of FL-NS was the porosity of the Es4x sandstone sample at 3671.8m in Well Tuo720. Densities of Quartz, K-feldspar, Albite, Dolomite, Kaolinite and pore water are 2.65×10^3 kg/m^3, 2.59×10^3 kg/m^3, 2.62×10^3 kg/m^3, 2.87×10^3 kg/m^3, 2.61×10^3 kg/m^3 and 1×10^3 kg/m^3, respectively.

Table 6. Ion composition of the solution in numerical simulations

Ion types	Concentration, mol/L		
	FW-NS	SHCa-NS	SLCa-NS
K^+	0.012	1×10^{-8}	0.012
Na^+	3.72	1×10^{-8}	3.72
Ca^{2+}	0.38	0.38	0.001
Mg^{2+}	0.053	1×10^{-8}	0.053
Cl^-	4.58	0.76	3.82
HCO_3^-	0.0043	1×10^{-8}	0.0043
SiO_2	1×10^{-8}	1×10^{-8}	1×10^{-8}
Al^{3+}	1×10^{-8}	1×10^{-8}	1×10^{-8}

Note: The concentration of KCl, NaCl, $CaCl_2$, $MgCl_2$, HCO_3^- in FW-NS was from the average ion concentration in formation water of the Es4x to Es3z in the Shengtuo area. The concentration of $CaCl_2$ in SHCa-NS was from the average ion concentration of $CaCl_2$ in the formation water of the Es4x to Es3z in the Shengtuo area. The concentration of KCl, NaCl, $MgCl_2$, HCO_3^- in SLCa-NS was from the average ion concentration in the formation water of the Es4x to Es3z in the Shengtuo area. The concentration of SiO_2, Al^{3+} in FW-NS, SHCa-NS and SLCa-NS, and concentration of NaCl and KCl in SHCa-NS were set to 1×10^{-8} mol/L to meet the low ion concentration and software requirements.

Table 7. Kinetic data of various minerals used for the numerical simulations

Minerals	K_{25}	E_a	K_{100}	K_{150}	*SSA*	*NC*	References
Calcite	1×10^{-9}	48.2	4.98×10^{-8}	3.12×10^{-7}	375	-	Arvidson et al., 2003; Pokrovsky et al., 2009
K-feldspar	1×10^{-17}	57.78	1.08×10^{-15}	9.78×10^{-15}	125	-	Kampman et al., 2009; Xu el al, 2005; Harouiya and Oelkers, 2004
Albite	1×10^{-18}	65	1.95×10^{-16}	2.31×10^{-15}	125	-	Palandri and Kharaka, 2004; Gonnenthal and Spyoher, 2001; Xu et al., 2005
Quartz	1.26×10^{-18}	87.5	1.52×10^{-15}	4.26×10^{-14}	125	110	Xu et al., 2005; Harouiya and Oelkers, 2004;
Kaolinite	1.26×10^{-17}	62.76	2.04×10^{-15}	2.23×10^{-14}	25000	620	Xu et al., 2005; Li et al., 2008
Dolomite	1.26×10^{-9}	62.76	2.04×10^{-7}	2.23×10^{-6}	125	-	Arvidson et al., 2003; Pokrovsky et al., 2009

Note: K_{25}, rate constant at 25°C, mol/cm^2/s. E_a, activation energy, K$_j$/mol. K_{100}, rate constant at 100°C, mol/cm^2/s. K_{150}, rate constant at 150°C, mol/cm^2/s. *SSA*, Specific surface area (cm^2/g). *NC*, Nucleus (cm^2/cm^3).

Table 8. XRD data of DLF-LE from the sandstone reservoirs of ES3z at 2938.13m in Well Tuo 76 and FL-LE from the sandstone reservoirs of ES4 at 3671.8m in Well Tuo 720 used in the laboratory experiments..

Minerals	XRD volume fraction (%) of DLF-LE	XRD volume fraction (%) of FL-LE
Quartz	40	52
K-feldspar	8	22
Albite	18	24
Dolomite	33	0
Kaolinite	1	2

Table 9. EDS data in Figs.4-6. AP: Atomic percentage, %; A5-F5: EDS data in Figs.4; A6-F6: EDS data in Figs.5; A7-G7: EDS data in Figs.6;

Element	Fe(AP)	Ca(AP)	Mg(AP)	C(AP)	O(AP)	Al(AP)	Si(AP)
A5	2.55	22.65	10.93	13.16	49.72	-	-
B5	8.36	25.22	10.6	7.52	41.41	-	-
C5	2.05	13.73	11.36	21.17	49.84	-	-

D5	6.5	58.45	8.07	8.59	40.91	-	-
E5	-	39.27	17.56	9.2	33.97	-	-
F5	-	32.57	20.23	10.43	36.77	-	-
A6	-	-	-	-	39.78	34.99	19.23
B6	-	-	-	-	31.63	30.28	26.5
C(GB)6	-	-	-	-	50.98	49.02	-
C(Kao)6	-	-	-	-	51.86	26.11	22.03
D6	-	-	-	-	59.8	20.38	19.82
E6	-	-	-	-	45.75	29.78	24.47
F6	-	-	-	-	42.41	57.59	-
A7	3.04	44.83	0.8	15.48	35.75	-	-
B7	3.39	44.58	2.05	14.04	35.52	-	-
C7	−	25.5	−	41.22	33.28	-	-
D7	−	31.83	−	17.12	51.05	-	-
E7	−	23.19	−	44.81	32	-	-
F7	−	27.29	−	44.37	28.34	-	-
G7	−	22.32	−	43.71	33.97	-	-
H7	−	26.3	−	43.45	30.25	-	-

Table 10. Chemical composition of the post-experiment solution in laboratory experiments. EXP, Experiments.

EXP	Al^{3+} (μmol/L)	Ca^{2+} (μmol/L)	Fe^{2+} (μmol/L)	K^{+} (μmol/L)	Mg^{2+} (μmol/L)	Na^{+} (μmol/L)	SiO_2(aq) (μmol/L)	HCO_3^- (μmol/L)	CO_3^{2-} (μmol/L)	Cl^- (μmol/L)	pH (25℃)
1	0.05	2322.5	0.4	22.18	1557.5	323	86.1	8490.3407	1.35×10−8	/	4.4
2	0.11	1024	0.21	61.72	693.75	313	848	7228.0889	1.61×10−8	/	4.6
3	1.29	1788.25	3.47	177.95	1034.17	1053	2135	15434.543	1.09×10−7	/	5.1
4	1.17	425500	118.79	305.38	285.46	6308.7	1437.33	104676.6	1.17×10−8	760000	3.3
5	0.77	382250	96.07	19351.28	22033.33	4395652.2	118.7	644365.25	2.87×10−7	4580000	3.9
6	0.21	472000	114.16	435.38	2321.25	10673.91	656.5	202686.17	1.43×10−7	760000	4.1

Table 11. Calculated saturation indices of the post-experiment solutions

Experiments	K-feldspars	Albite	Quartz	Kaolinite	Calcite	Dolomite	Gibbsite
1	−5.59	−8.21	−1.08	1.56	−1.06	−5.8	4.25
2	−3.90	−6.38	−0.46	0.53	−0.74	−5.19	5.17
3	−1.16	−3.57	−0.06	2.49	0.5	−3.27	7.75
4	−1.48	−2.36	−0.23	6.32	−0.29	−5.99	2.31
5	−3.11	−2.95	−1.32	2.59	0.87	−2.35	3.93
6	−3.1	−3.9	−0.57	2.55	1.36	−2.63	3.96

Table 12. Concentration of CO_2 dissolved into the solution in all the numerical simulations .

numerical simulations	Time, years	CO_2(aq), mol/L	CO_3^{2-}, (mol/L)	HCO_3^-, mol/L	TCC
1	1000	0.37	5.34×10^{-6}	0.079	0.449
2	1000	0.37	1.43×10^{-5}	0.086	0.456
3	1000	0.41	9.38×10^{-5}	0.31	0.72
4	1000	0.38	8.65×10^{-6}	0.092	0.472
5	1000	0.38	8.85×10^{-6}	0.093	0.473

Note: TCC, Total concentration of CO_2 dissolved into the solution, mol/L

Table 13. Mineral saturation indices (lg (Q/K)) at the initial time of the numerical simulations

Simulations	Albite	Dolomite	K-feldspars	Kaolinite	Quartz
1	−34.52	0.86	−34.99	−29.79	−9.36
2	−34.52	/	−34.99	−29.79	−9.36
3	−48.38	−11.11	−46.36	−36.51	−9.57
4	−34.22	−0.88	−34.69	−29.54	−9.37

Table 14. Mineral reaction rates at the initial time of the numerical simulations. NS, numerical simulations; Ca, Calcite; KF, K-feldspar; P, Albite; Q, Quartz; Kao, Kaolinite; Dol, Dolomite.

NS	Ca, mol/kg/s	KF, mol/kg/s	P, mol/kg/s	Q, mol/kg/s	Kao, mol/kg/s	Dol mol/kg/s
1	−0.0034	2.6×10^{-10}	1.04×10^{-10}	0	0	−0.44
2	−0.00034	5.18×10^{-10}	1.03×10^{-10}	0	0	/
3	0.014	2.6×10^{-10}	1.04×10^{-10}	0	0	0.07
4	0.014	2.6×10^{-10}	1.04×10^{-10}	0	0	0.061

Table 15. Final dissolution and precipitation mass of minerals after 1000 years in numerical simulations. Negative value denotes precipitation mass and positive value denotes dissolution mass.

Simulations	Calcite, kg	Dolomite, kg	K-feldspar, kg	Albite, kg	Quartz, kg	Kaolinite, kg
1	−5.79	1.514	3.748	35.76	−16.98	−18.24
2	−5.80		3.633	31.86	−15.17	−16.30
3	−5.27	0.33	3.258	38.51	−17.81	−19.14
4	−0.81	2.05	1.631	5.79	−3.10	−3.33
5	−11.27	3.41	14.57	83.28	−39.66	−42.58

Table 16. Quantity of geologic CO_2 storage in the numerical simulations within 1000 years. NS, numerical simulations; ST, Solubility trapping; MT, Mineral trapping. TCSC, Total CO_2 storage capacity

NS	CO_2(aq), kg/m^3	HCO_3^-+CO_3^{2-}, kg/m^3	ST, kg/m^3	MT, kg/m^3	TCSC, kg/m^3
1	2.48	0.53	3.01	2.54	5.55
2	2.49	0.58	3.07	2.55	5.62
3	2.48	1.87	4.35	2.32	6.67
4	2.53	0.61	3.14	0.35	3.49
5	5.76	1.42	7.18	4.95	12.13

Appendix 2. Boundary conditions of numerical simulations

① NUMERICAL SIMULATION 1:

Constraints on initial system:

Temperature = 150°C

H_2O=127.6 kg

Cl^- = 4.58 mol/L

Ca^{2+} = 0.38 mol/L

HCO^-_3 = 0.0043 mol/L charge balance

K^+= 0.012 mol/L

Al^{3+}= 0.00000001 mol/L

SiO_2(aq) = 0.00000001 mol/L

Swap CO_2(g) for H^+

Fix CO_2(g) = 4 MPa

Reactants:

Calcite = 0 kg, kinetic Calcite rate constant = 3.12×10^{-7} mol cm^{-2} s^{-1}, surface area = 375 cm^2 g^{-1}

K-feldspar = 248.55 kg, kinetic K-feldspar rate constant = 9.78×10^{-15} mol cm^{-2} s^{-1}, surface area= 125 cm^2 g^{-1}

Kaolinite = 106.33 kg, kinetic Kaolinite rate constant = 2.23×10^{-14} mol cm^2 s^{-1}, surface area = 25000 cm^2 g^{-1}, nucleus =620 cm^2/cm^3

Quartz = 975.46 kg, kinetic Quartz rate constant= 4.26×10^{-14} mol cm^2 s^{-1}, surface area= 125 cm^2 g^{-1}, nucleus = 110 cm^2/cm^3

Albite = 548.57 kg, kinetic Albite rate constant= 2.31×10^{-15} mol cm^2 s^{-1}, surface area= 125 cm^2 g^{-1}

Dolomite = 455.69 kg, kinetic Dolomite rate constant= 2.23×10^{-6} mol cm^2 s^{-1}, surface area= 125 cm^2 g^{-1}

Other constraints:

Suppress Illite

Suppress "Maximum Microcline"

Time Start = 0 y, End = 1000 y

② NUMERICAL SIMULATION 2:

Constraints on initial system:

Temperature = 150°C

H_2O=131 kg

Cl^- = 4.58 mol/L

Ca^{2+} = 0.38 mol/L

HCO^-_3 = 0.0043 mol/L charge balance

K^+= 0.012 mol/L

Al^{3+}= 0.00000001 mol/L

$SiO_2(aq)$ = 0.00000001 mol/L

Swap $CO_2(g)$ for H^+

Fix $CO_2(g)$ = 4 MPa

Reactants:

Calcite = 0 kg, kinetic Calcite rate constant = 3.12×10^{-7} mol cm^{-2} s^{-1}, surface area = 375 cm^2 g^{-1}

K-feldspar =495.16 kg, kinetic K-feldspar rate constant = 9.78×10^{-15} mol cm^{-2} s^{-1}, surface area= 125 cm^2 g^{-1}

Kaolinite = 45.36 kg, kinetic Kaolinite rate constant = 2.23×10^{-14} mol cm^2 s^{-1}, surface area = 25000 cm^2 g^{-1}, nucleus =620 cm^2/cm^3

Quartz = 1199.29 kg, kinetic Quartz rate constant= 4.26×10^{-14} mol cm^2 s^{-1}, surface area= 125 cm^2 g^{-1}, nucleus = 110 cm^2/cm^3

Albite = 546.43 kg, kinetic Albite rate constant= 2.31×10^{-15} mol cm^2 s^{-1}, surface area= 125 cm^2 g^{-1}

Dolomite = 0 kg, kinetic Dolomite rate constant= 2.23×10^{-6} mol cm^2 s^{-1}, surface area= 125 cm^2 g^{-1}

Other constraints:

Suppress Illite

Suppress "Maximum Microcline"

Time Start = 0 y, End = 1000 y

③ NUMERICAL SIMULATION 3:

Constraints on initial system:

Temperature = 150°C
H_2O=127.6 kg
Cl^- = 0.76 mol/L
Ca^{2+} = 0.38 mol/L
HCO^-_3 = 0.00000001 mol/L charge balance
K^+= 0.00000001 mol/L
Al^{3+}= 0.00000001 mol/L
SiO_2(aq) = 0.00000001 mol/L
Swap CO_2(g) for H^+
Fix CO_2(g) = 4 MPa
Reactants:
Calcite = 0 kg, kinetic Calcite rate constant = 3.12×10^{-7} mol cm^{-2} s^{-1}, surface area = 375 cm^2 g^{-1}
K-feldspar = 248.55 kg, kinetic K-feldspar rate constant = 9.78×10^{-15} mol cm^{-2} s^{-1}, surface area= 125 cm^2 g^{-1}
Kaolinite = 106.33 kg, kinetic Kaolinite rate constant = 2.23×10^{-14} mol cm^2 s^{-1}, surface area = 25000 cm^2 g^{-1}, nucleus =620 cm^2/cm^3
Quartz = 975.46 kg, kinetic Quartz rate constant= 4.26×10^{-14} mol cm^2 s^{-1}, surface area= 125 cm^2 g^{-1}, nucleus = 110 cm^2/cm^3
Albite = 548.57 kg, kinetic Albite rate constant= 2.31×10^{-15} mol cm^2 s^{-1}, surface area= 125 cm^2 g^{-1}
Dolomite = 455.69 kg, kinetic Dolomite rate constant= 2.23×10^{-6} mol cm^2 s^{-1}, surface area= 125 cm^2 g^{-1}
Other constraints:
Suppress Illite
Suppress "Maximum Microcline"
Time Start = 0 y, End = 1000 y

④ NUMERICAL SIMULATION 4:
Constraints on initial system:
Temperature = 150°C
H_2O=127.6 kg
Cl^- = 3.82 mol/L
Ca^{2+} = 0.001 mol/L
HCO^-_3 = 0.0043 mol/L charge balance
K^+= 0.012 mol/L
Al^{3+}= 0.00000001 mol/L
SiO_2(aq) = 0.00000001 mol/L
Swap CO_2(g) for H^+
Fix CO_2(g) = 4 MPa
Reactants:
Calcite = 0 kg, kinetic Calcite rate constant = 3.12×10^{-7} mol cm^{-2} s^{-1}, surface area = 375 cm^2 g^{-1}
K-feldspar = 248.55 kg, kinetic K-feldspar rate constant = 9.78×10^{-15} mol cm^{-2} s^{-1}, surface area= 125 cm^2 g^{-1}
Kaolinite = 106.33 kg, kinetic Kaolinite rate constant = 2.23×10^{-14} mol cm^2 s^{-1}, surface area = 25000 cm^2 g^{-1}, nucleus =620 cm^2/cm^3

Quartz = 975.46 kg, kinetic Quartz rate constant= 4.26×10^{-14} mol cm^2 s^{-1}, surface area= 125 cm^2 g^{-1}, nucleus = 110 cm^2/cm^3

Albite = 548.57 kg, kinetic Albite rate constant= 2.31×10^{-15} mol cm^2 s^{-1}, surface area= 125 cm^2 g^{-1}

Dolomite = 455.69 kg, kinetic Dolomite rate constant= 2.23×10^{-6} mol cm^2 s^{-1}, surface area= 125 cm^2 g^{-1}

Other constraints:

Suppress Illite

Suppress "Maximum Microcline"

Time Start = 0 y, End = 1000 y

⑤ NUMERICAL SIMULATION 5:

Constraints on initial system:

Temperature = 150℃

H_2O=299 kg

Cl^- = 4.58 mol/L

Ca^{2+} = 0.38 mol/L

HCO^-_3 = 0.0043 mol/L charge balance

K^+= 0.012 mol/L

Al^{3+}= 0.00000001 mol/L

$SiO_2(aq)$ = 0.00000001 mol/L

Swap $CO_2(g)$ for H^+

Fix $CO_2(g)$ = 4 MPa

Reactants:

Calcite = 0 kg, kinetic Calcite rate constant = 3.12×10^{-7} mol cm^{-2} s^{-1}, surface area = 375 cm^2 g^{-1}

K-feldspar =546 kg, kinetic K-feldspar rate constant = 9.78×10^{-15} mol cm^{-2} s^{-1}, surface area= 125 cm^2 g^{-1}

Kaolinite =91 kg, kinetic Kaolinite rate constant = 2.23×10^{-14} mol cm^2 s^{-1}, surface area = 25000 cm^2 g^{-1}, nucleus =620 cm^2/cm^3

Quartz = 988 kg, kinetic Quartz rate constant= 4.26×10^{-14} mol cm^2 s^{-1}, surface area= 125 cm^2 g^{-1}, nucleus = 110 cm^2/cm^3

Albite = 520 kg, kinetic Albite rate constant= 2.31×10^{-15} mol cm^2 s^{-1}, surface area= 125 cm^2 g^{-1}

Dolomite =156 kg, kinetic Dolomite rate constant= 2.23×10^{-6} mol cm^2 s^{-1}, surface area= 125 cm^2 g^{-1}

Other constraints:

Suppress Illite

Suppress "Maximum Microcline"

Time Start = 0 y, End = 1000 y

Appendix 3. Model parameters of numerical simulations

The masses of water and rock in the reaction simulations defines the water: rock ratio. The default simulation mass is the sum of minerals mass and pore water mass. The mineral mass equaled the product of minerals density (Table 5) and relative weight percent of that mineral as determined from the XRD analysis. The pore water mass equaled the product of water density (Table 5) and measured porosity from the sandstone samples in the Shengtuo area (Table 5).

The CO_2 solubility were determined with an online calculator using input values of reservoir temperature, pressure, and molar concentration of $CaCl_2$, NaCl, $MgCl_2$, KCl in the formation water. GWB simulations of CO_2 solubility are based on activities calculated by both the Davies and Pitzer equations (Duan et al., 1992; Duan and Mao, 2006; Zerai et al., 2009). These models of CO_2 solubility use a modified Henry's law to describe the partitioning of CO2 between gas and aqueous phases.

GWB simulations of activity models are based on activities calculated by both the Davies and Pitzer equations (Zerai et al., 2009). The GWB can be set to correct the activity coefficient of CO_2 for the temperature and the ionic strength of solution by using a polynomial fit to experimental data developed by Helgeson [1969]. By default, activity coefficients for neutral species such as CO_2 are set to one. GWB can be set to use the Helgeson [1969] formulation for the activity coefficient by setting the ionic size to -0.5. The ion size parameter has a special meaning for neutrally charged aqueous species in the GWB thermodynamic data set and determines which formulation for the activity coefficient is used. The activity model was used in many simulation studies (Duan et al., 1992; Duan and Mao, 2006; Zerai et al., 2009; Saylor et al., 2009), indicating thermodynamic database used in the GWB simulations with an appropriate activity correction model.

Table 17 Model parameters of numerical simulations

Parameter	Symbol	Units
reaction rate	r_m	mol/s
rate constant	k_m	mol/cm^2/s
surface area of minerals	A_m	cm^2
activity product for the dissolution reaction	Q	/
equilibrium constant for the dissolution reaction	K	/
rate constant at 25℃	k_{25}	mol/cm^2/s
rate constant at 100℃	k_{100}	mol/cm^2/s
rate constant at 150℃	k_{150}	mol/cm^2/s
activation energy	E_a	kj/mol
gas constant	R	/
the absolute temperature	T	K
Specific surface area	SSA	cm^2/g
Nucleus	NC	cm^2/cm^3
Equilibrium constants	K_{eq}	/
partial pressure of carbon dioxide	P_{CO2}	MPa
saturation indices	SI	/